JACS
JOURNAL OF THE AMERICAN CHEMICAL SOCIETY
Article
Cite This: J. Am. Chem. Soc. 2019, 141, 15046−15057
pubs.acs.org/JACS

How Metal Ion Lewis Acidity and Steric Properties Influence the Barrier to Dioxygen Binding, Peroxo O−O Bond Cleavage, and Reactivity

Penny Chaau Yan Poon,[‡] Maksym A. Dedushko,[‡] Xianru Sun,[∥] Guang Yang,[∥] Santiago Toledo,[§] Ellen C. Hayes,[‡] Audra Johansen,[‡] Marc C. Piquette,[∥] Julian A. Rees,[⊥] Stefan Stoll,[‡] Elena Rybak-Akimova,[∥,†] and Julie A. Kovacs*[,‡]

[‡]Department of Chemistry, University of Washington, Campus Box 351700, Seattle, Washington 98195-1700, United States
[§]The Department of Chemistry, St. Edward's University, 3001 South Congress, Austin, Texas 78704-6489, United States
[∥]Department of Chemistry, Tufts University, 62 Talbot Avenue, Medford, Massachusetts 02155, United States
[⊥]Chemical Sciences Division, Lawrence Berkeley National Laboratory, Berkeley, California 94720, United States

Supporting Information

ABSTRACT: Herein we quantitatively investigate how metal ion Lewis acidity and steric properties influence the kinetics and thermodynamics of dioxygen binding versus release from structurally analogous Mn−O_2 complexes, as well as the barrier to Mn peroxo O−O bond cleavage, and the reactivity of Mn oxo intermediates. Previously we demonstrated that the steric and electronic properties of Mn^{III}−OOR complexes containing N-heterocyclic (N^{Ar}) ligand scaffolds can have a dramatic influence on alkylperoxo O−O bond lengths and the barrier to alkylperoxo O−O bond cleavage. Herein, we examine the dioxygen reactivity of a new Mn^{II} complex containing a more electron-rich, less sterically demanding N^{Ar} ligand scaffold, and compare it with previously reported Mn^{II} complexes. Dioxygen binding is shown to be reversible with complexes containing the more electron-rich metal ions. The kinetic barrier to O_2 binding and peroxo O−O bond cleavage is shown to correlate with redox potentials, as well as the steric properties of the supporting N^{Ar} ligands. The reaction landscape for the dioxygen chemistry of the more electron-rich complexes is shown to be relatively flat. A total of four intermediates, including a superoxo and peroxo species, are observed with the most electron-rich complex. Two new intermediates are shown to form following the peroxo, which are capable of cleaving strong X−H bonds. In the absence of a sacrificial H atom donor, solvent, or ligand, serves as a source of H atoms. With TEMPOH as sacrificial H atom donor, a deuterium isotope effect is observed (k_H/k_D = 3.5), implicating a hydrogen atom transfer (HAT) mechanism. With 1,4-cyclohexadiene, 0.5 equiv of benzene is produced prior to the formation of an EPR detected $Mn^{III}Mn^{IV}$ bimetallic species, and 0.5 equiv after its formation.

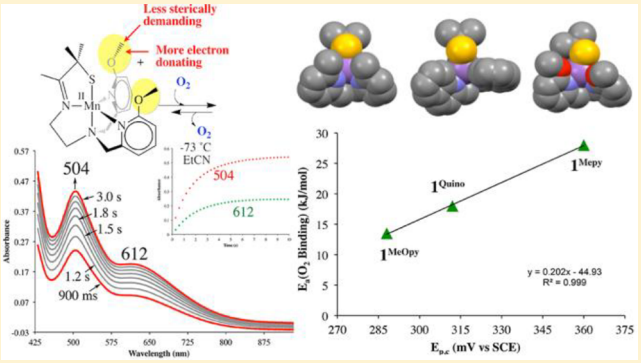

INTRODUCTION

Fundamental scientific research is needed in order to develop methods for efficiently capturing sunlight, and converting its energy into storable fuels. Nature accomplishes this via photosynthesis, which converts solar energy into energy that is stored in a chemical bond by extracting electrons from H_2O to form O_2.[1−4] The sluggish kinetics of H_2O oxidation has been a major concern for existing fuel cells.[5] Nature had a few billion years to refine its Mn-containing photosynthetic H_2O oxidation catalyst, therefore understanding the mechanism by which it facilitates this reaction, or its microscopic reverse, would be of value. However, despite its relevance to photosynthesis,[6−9] the dioxygen chemistry of Mn remains relatively unexplored,[6,10−12] relative to that of Fe and Cu.[13−19] Very little is known about the photosynthetic Mn-induced O−O bond forming step,[20] because it occurs following the rate-determining step.[21−25] An unobserved peroxo intermediate is proposed to form,[22−24] which then readily evolves O_2.[26]

Previously we showed that coordinatively unsaturated $[Mn^{II}(L^{Mepy})]^+$ ($\mathbf{1}^{Mepy}$, L^{Mepy} = (6-Me-DPEN)$N_4{}^{Me2}S^-$) reacts with O_2 at low temperatures (−40 °C) to form dioxygen-bound $[Mn(L^{Mepy})(O_2)]^+$ ($\mathbf{2}^{Mepy}$), en route to the first example of a crystallographically characterized binuclear peroxo-bridged dimer, $\{[Mn^{III}(L^{Mepy})]_2(\mu\text{-}O_2)\}^{2+}$ ($\mathbf{3}^{Mepy}$).[6] Dioxygen binding to $\mathbf{1}^{Mepy}$ was shown to occur on the millisecond time-scale.[6] A thiolate was incorporated into our ligand scaffold in order to (1) provide a chromophore that facilitates the spectroscopic

Received: May 2, 2019
Published: September 3, 2019

DOI: 10.1021/jacs.9b04729
J. Am. Chem. Soc. 2019, 141, 15046−15057

observation of metastable intermediates,[6,27−31] (2) lower the activation barrier to O_2 binding, and (3) provide stability to M−O_2 species.[32,33] The rate at which peroxo-bridged $\mathbf{3}^{\mathbf{Mepy}}$ forms is slow enough at −40 °C to monitor using a benchtop UV−vis spectrometer. However, with the L^{Mepy} ligand system it was not possible to determine the mechanism by which the O−O bond of peroxo-bridged $\mathbf{3}^{\mathbf{Mepy}}$ cleaves to afford mono-oxo bridged Mn^{III}−O−Mn^{III} ($\mathbf{6}^{\mathbf{Mepy}}$, Figure 1), because this step was shown

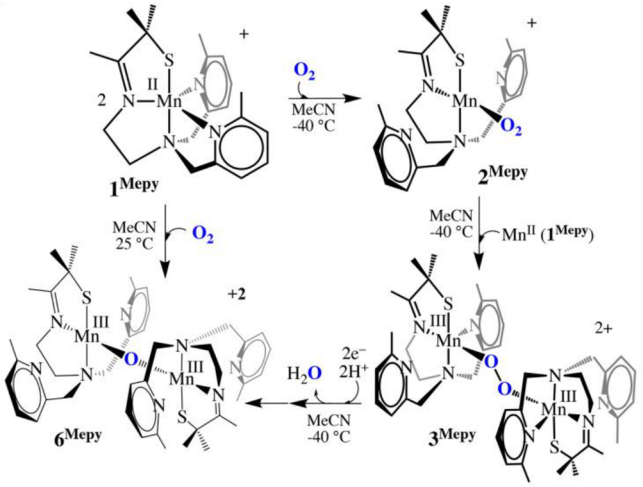

Figure 1. Low temperature reaction between $\mathbf{1}^{\mathbf{Mepy}}$ and O_2 affords $\mathbf{6}^{\mathbf{Mepy}}$ via observable superoxo $\mathbf{2}^{\mathbf{Mepy}}$ and peroxo $\mathbf{3}^{\mathbf{Mepy}}$ intermediates.

to be rate-determining.[6] Mechanisms for O−O bond cleavage with Fe and Cu have been shown to involve either protonation of a M−OOH at the distal oxygen,[34] or the addition of a second metal ion to the distal oxygen to form a bridging peroxo. Ideally an η^2,η^2-side-on peroxo forms so as to maximize overlap with the empty σ^*(O−O).[14,19] In contrast, mechanistic details regarding Mn-promoted O−O bond cleavage versus formation remain relatively unexplored.[35−41] An end-on peroxo complex is expected to be more stable than a side-on peroxo complex, perhaps explaining why we were able to crystallize $\mathbf{3}^{\mathbf{Mepy}}$. Prior to our work,[6] there were no characterized examples of binuclear end-on or side-on Mn^{III}-peroxos, and there were only a handful of examples of monomeric η^2-side-on Mn^{III}-peroxos,[10,42−45] only one of which is derived from O_2.[10] An end-on Mn^{III}−OOH was shown to form upon protonation of the corresponding η^2-side-on Mn^{III}-peroxo compound; however, it was not crystallographically characterized.[46]

A series of structurally analogous five-coordinate, thiolate-ligated Mn^{II} complexes (e.g., $\mathbf{1}^{\mathbf{Mepy}}$ of Figure 1) was previously reported by our group, which incorporate readily derivatized N-heterocycle amines (N^{Ar} = 6-H-pyridine ($\mathbf{1}^{\mathbf{py}}$), 6-Me-pyridine ($\mathbf{1}^{\mathbf{Mepy}}$), and quinoline ($\mathbf{1}^{\mathbf{Quino}}$)), providing us with a method for tuning their steric and electronic properties.[6,47] In order to obtain more information regarding the mechanism of the O−O bond cleaving step, we explore herein the low-temperature dioxygen chemistry of quinoline-ligated $[Mn^{II}(L^{Quino})]^+$ ($\mathbf{1}^{\mathbf{Quino}}$),[48] in addition to that of a new Mn^{II} complex, $[Mn^{II}(L^{MeOpy})]^+$ ($\mathbf{1}^{\mathbf{MeOpy}}$), containing a more electron donating substituent on the pyridine ring. We will show that the barrier to selected steps of the reaction, including O_2 binding and release, and O−O bond cleavage, can be adjusted by changing the electron donor character of the ligand.[47]

RESULTS AND DISCUSSION

Rationale for the ligand design of the complexes studied herein stems in part from a previous study in which a correlation between peroxo O−O bond lengths and Mn···N^{Ar} distances (N^{Ar} = N-heterocycle) was observed with a series of alkylperoxo $^{Quino,Mepy}LMn^{III}$−OOR (R = ^{t}Bu, Cm) compounds.[49] We refer to the interaction between the Mn ion and the N^{Ar} ligand as Mn···N^{Ar}, because, although not within bonding distance, the N^{Ar} ligand was shown (by X-ray crystallography) to point directly toward the metal ion, and (by spectroscopic methods) to influence properties of the complex in a systematic way. A decrease in the mean Mn···N^{Ar} distance (from 2.510 to 2.411 Å) was found to elongate the peroxo O−O bond (from 1.431 to 1.468 Å).[6,7] In addition, the kinetic barrier to alkylperoxo O−O bond cleavage ($\Delta H^{\ddagger}$) was shown to directly correlate with the Mn···N^{Ar} distance. At ambient temperatures, dioxygen was shown to react with the Mn^{II} precursors ($\mathbf{1}$) to form fairly stable bimetallic mono oxo-bridged Mn^{III} complexes, (e.g., $\mathbf{6}^{\mathbf{Mepy}}$ of Figure 1) in high yields (96−98%).[6,48] Comparison of the mean Mn···N^{Ar} distance (Table 1) in these mono oxo-bridged

Table 1. Mean Crystallography-Determined Mn···N^{Ar} Distance for Bimetallic Mono Oxo-Bridged Mn^{III} Complexes, 6

N^{Ar}	complex	Mn···N^{Ar}_{avg} (Å)
6-H-pyridine	$\mathbf{6}^{\mathbf{py}}$	2.23(1)
6-MeO-pyridine	$\mathbf{6}^{\mathbf{MeOpy}}$	2.413(3)
Quinoline	$\mathbf{6}^{\mathbf{Quino}}$	2.5(1)
6-Me-pyridine	$\mathbf{6}^{\mathbf{Mepy}}$	2.56(2)

products provides us with a predictive metric that potentially reflects the O−O bond cleaving properties of the ligand. The Mn···N^{Ar} distance was shown to depend upon the steric properties of the N^{Ar} ligand scaffold.[11,49] Inspection of space filling models shows that the substituent in the 6-position of the pyridine ring clashes with one of the gem-dimethyls adjacent to the thiolate sulfur. This prevents the pyridine nitrogen from approaching the metal to the optimum Mn^{III}−N^{Ar} bond distance, if the substituent is larger than a hydrogen. With a hydrogen in the 6-position, the Mn−N^{Ar} distance is within the normal bonding range (Table 1), and thus the use of a single line to represent a bond. With larger substituents, the Mn···N^{Ar} separation is well outside the normal bonding range. For example, with a Me-group, the Mn···N^{Ar}_{avg} separation is 0.33 Å longer than that of the less sterically encumbered 6-H derivative, $\mathbf{6}^{\mathbf{py}}$ (Table 1), resulting in a more Lewis acidic metal ion. If this is extrapolated to the corresponding peroxo compounds, the more Lewis acidic metal ion associated with bulkier substituents would strengthen π-interaction metal, and therefore shift electron density out of the peroxo π^*(O−O) into the Mn−O π-bonding region, thereby strengthen the peroxo O−O bond.[49] Conversely, the shorter Mn^{III}−N^{Ar} bond associated with 6-H-pyridine would create a more electron rich Mn ion, thereby weakening the peroxo O−O bond, and facilitating its cleavage. Consistent with this, no intermediates are observed in the reaction between O_2 and $[Mn^{II}(L^{py})]^+$ ($\mathbf{1}^{\mathbf{py}}$),[48] even at temperatures as low as −78 °C, whereas peroxo compound $\mathbf{3}^{\mathbf{Mepy}}$ (Figure 1) is stable enough to crystallize. In order to obtain more information regarding the O−O bond-cleaving step, we turned to ligand systems (Scheme 1) that support a Mn···N^{Ar} separation in the crystallographically characterized binuclear oxo-bridged, $\{[Mn^{III}(L^{NAr})]_2$-$(\mu$-O)$\}^{2+}$ ($\mathbf{6}$), which is shorter

DOI: 10.1021/jacs.9b04729
J. Am. Chem. Soc. 2019, 141, 15046−15057

Scheme 1. Low Temperature Reaction between 1 and O_2 Affords Mono Oxo Bridged 6 via Observable Superoxo, 2, and Peroxo, 3, Intermediates[a]

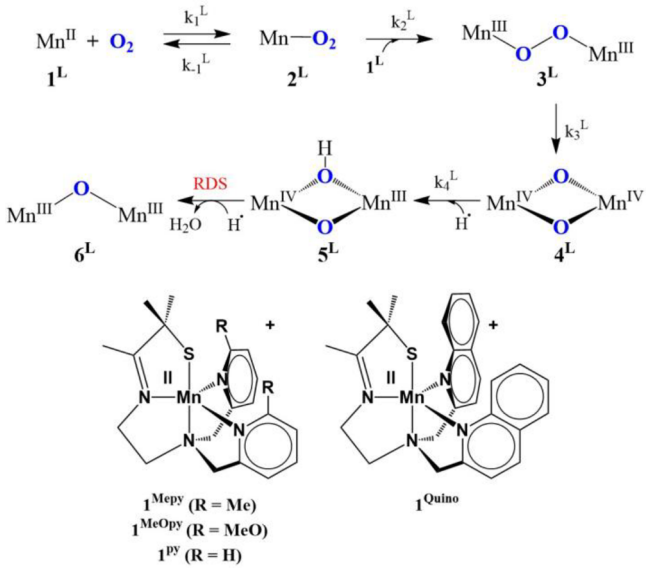

[a]L= py, Mepy, MeOpy, and Quino.

than 6-Me-pyridine $\mathbf{6}^{\mathbf{Mepy}}$, but longer than pyridine $\mathbf{6}^{\mathbf{py}}$. Distances in **6** were used as a predictive parameter, since we do not have structures for all of the peroxo compounds. Quinoline $\{[Mn^{III}(L^{Quino})]_2\text{-}(\mu\text{-}O)\}^{2+}$ ($\mathbf{6}^{\mathbf{Quino}}$)[48] and 6-MeO-pyridine $\{[Mn^{III}(L^{MeOpy})]_2\text{-}(\mu\text{-}O)\}^{2+}$ ($\mathbf{6}^{\mathbf{MeOpy}}$) both fit this criterion (Table 1). Below, we examine the temperature-dependent kinetics of the reaction between O_2 and the Mn^{II} precursors to $\mathbf{6}^{\mathbf{Quino}}$ and $\mathbf{6}^{\mathbf{MeOpy}}$, $[Mn^{II}(L^{Quino})]^+$ ($\mathbf{1}^{\mathbf{Quino}}$) and $[Mn^{II}(L^{MeOpy})]^+$ ($\mathbf{1}^{\mathbf{MeOpy}}$), respectively (Scheme 1). We will show that the relative stability and reactivity of metastable intermediates, and the barriers to O_2 binding or release, and peroxo O—O bond cleavage, is highly dependent on the supporting ligands. By changing the solvents and corresponding solvent C—H bond strength, or by adding a sacrificial H atom donor, we are able to spectroscopically observe two new intermediates, each of which is capable of abstracting H atoms from strong X—H bonds (X = C, or O).

Reactivity of $\mathbf{1}^{\mathbf{Quino}}$ with Dioxygen. The low-temperature (−73 °C) reaction between colorless $[Mn^{II}(L^{Quino})]^+$ ($\mathbf{1}^{\mathbf{Quino}}$)[48] and O_2 affords a metastable green intermediate, $\mathbf{3}^{\mathbf{Quino}}$, which rapidly converts to mono oxo-bridged $\mathbf{6}^{\mathbf{Quino}}$ (λ_{max} = 580 nm).[48] The stability of $\mathbf{3}^{\mathbf{Quino}}$ is temperature-dependent. In CH_3CN (f.p. = −40 °C, C—H BDE = 93 kcal/mol), metastable $\mathbf{3}^{\mathbf{Quino}}$ decays in ∼30 s at −40 °C, and is therefore best observed using a stopped-flow instrument. In CH_2Cl_2 (f.p. = −90 °C, C—H BDE = 98 kcal/mol), on the other hand, intermediate $\mathbf{3}^{\mathbf{Quino}}$ is more stable at −90 °C ($t^{3Quino\rightarrow 6Quino}$ = 7 min) making it possible to obtain a spectrum using a benchtop UV—vis spectrometer (Figure 2). Given the close similarity of its electronic absorption spectrum to that of peroxo-bridged $\mathbf{3}^{\mathbf{Mepy}}$ (λ_{max} = 640 nm),[6] it was deemed likely that $\mathbf{3}^{\mathbf{Quino}}$ is also a peroxo-bridged dimer, $\{[Mn^{III}(L^{Quino})]_2(\mu\text{-}O_2)\}^{2+}$($\mathbf{3}^{\mathbf{Quino}}$). This is supported by a low-resolution crystal structure (Figure S1), the connectivity of which indicates that there are two bridging oxygens (Table S1). In addition, 0.48 equiv of H_2O_2 are released per Mn ion upon the addition of 1.34 equiv of H_2SO_4 to $\mathbf{3}^{\mathbf{Quino}}$ (see assay conditions in SI) consistent with a peroxo-bridged dimer. Metrical

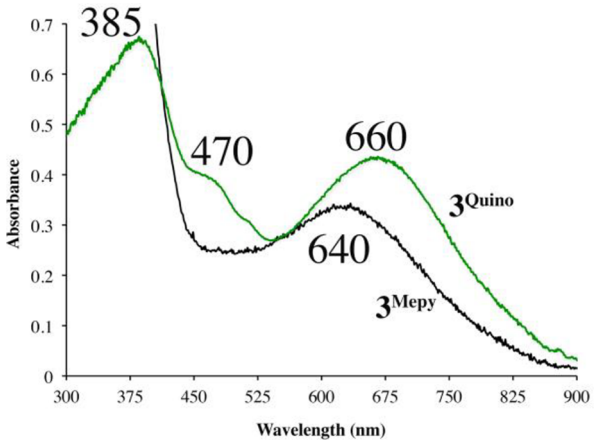

Figure 2. Electronic absorption spectrum of putative peroxo $\mathbf{3}^{\mathbf{Quino}}$ (green) generated via the addition of O_2 to 1.0 mM $\mathbf{1}^{\mathbf{Quino}}$ in CH_2Cl_2 at −73 °C, and $\mathbf{3}^{\mathbf{Mepy}}$ (black) generated via the addition of O_2 to 0.9 mM $\mathbf{1}^{\mathbf{Mepy}}$ and O_2 in CH_3CN at −40 °C.

parameters (Table S2) of the DFT optimized structure (Figure 3), calculated using the spin-unrestricted B3LYP hybrid

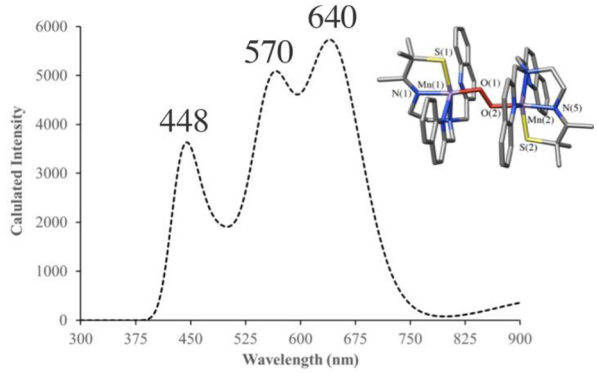

Figure 3. Time-dependent density functional theory (TD DFT) calculated electronic absorption spectrum of peroxo-bridged $\mathbf{3}^{\mathbf{Quino}}$ and its DFT optimized structure (using a B3LYP spin-unrestricted hybrid functional, and 6-311G basis set).

functional and the 6-311G basis set, are consistent with a *trans*-μ-1,2-peroxo-bridged Mn^{III}_2 dimer (O—O = 1.516 Å, Mn(1)—O(1) = 1.856 Å, Mn(2)—O(2) = 1.846 Å, Mn—S_{avg} = 2.35 Å, Mn(1)···Mn(2) = 4.244 Å, Mn—O—O_{avg} = 101°). The time-dependent DFT (TD-DFT) calculated electronic absorption spectrum (Figure 3) is in good agreement with the experimental spectrum (Figure 2). Transition-difference density plots show that these bands correspond to charge transfer transitions, and involve a mixed peroxo/thiolate → Mn(d) transition at higher energies and a thiolate → Mn(d) transition at lower energies (Figure S2). The calculated exchange coupling constant, J^{calc} = 3.8 cm^{-1}, indicates that the two Mn^{III} ions are essentially uncoupled. The calculated peroxo O—O bond length of $\mathbf{3}^{\mathbf{Quino}}$ is 0.06 Å longer than the crystallographically determined O—O bond of peroxo-bridged $\mathbf{3}^{\mathbf{Mepy}}$ (1.452(5) Å),[6] indicating that this bond should be more readily cleaved in $\mathbf{3}^{\mathbf{Quino}}$.

Temperature-Dependent Kinetics for the Formation of Peroxo $\mathbf{3}^{\mathbf{Quino}}$. Kinetics data for the formation of peroxo $\mathbf{3}^{\mathbf{Quino}}$ and its subsequent conversion to mono-oxo bridged $\mathbf{6}^{\mathbf{Quino}}$ (Scheme 1), were collected at low temperatures using a

DOI: 10.1021/jacs.9b04729
J. Am. Chem. Soc. 2019, 141, 15046−15057

stopped-flow instrument. The build-up and decay of $\mathbf{3}^{\mathbf{Quino}}$ was followed at 749 nm, where interference from $\mathbf{6}^{\mathbf{Quino}}$ is minimal. As illustrated in the time-resolved electronic absorption spectra of Figure S3, intermediate $\mathbf{3}^{\mathbf{Quino}}$ forms in less than 10 s at −20 °C (blue trace, λ_{max} = 652 nm) en route to the purple mono oxo bridged product, $\mathbf{6}^{\mathbf{Quino}}$ (pink trace, λ_{max} = 565 nm). No additional intermediates, prior to $\mathbf{3}^{\mathbf{Quino}}$, or in between $\mathbf{3}^{\mathbf{Quino}}$ and $\mathbf{6}^{\mathbf{Quino}}$, were detected with this particular ligand system (vide infra). The general kinetic scheme reflecting the two spectrophotometrically observed processes is shown in eqs 1 and 2 below. Under pseudo-first-order conditions, in the presence of excess O_2, kinetic traces could be fit to the biexponential eq 3, affording the pseudo-first-order rate constants ($k_{1,obs}{}'^{Quino}$ and $k_{3,obs}{}^{Quino}$) of eqs 1 and 2, respectively. Residuals were slightly larger for fits to a single exponential relative to fits to a biexponential. The observed rate constant for eq 1, $k_{1obs}{}'^{Quino}$, was found to increase linearly (Table S3) with increasing O_2 concentration (Figure S4), indicating that the reaction is first order with respect to $[O_2]$. The second-order rate constant ($k_1{}'^{Quino}$) was obtained from the slope of $k_{1,obs}{}'^{Quino}$ vs $[O_2]$ plots (Table 2) at four different temperatures. The

Table 2. Experimentally Obtained Rate Constants and Activation Parameters for the Formation of Peroxo-Bridged $\mathbf{3}^{\mathbf{Quino}}$ ($k_1{}'^{Quino}$), from $\mathbf{1}^{\mathbf{Quino}}$ (0.30 mM) + O_2 (4.1 mM) in CH_3CN, and Its Conversion to Mono Oxo-Bridged $\mathbf{6}^{\mathbf{Quino}}$ ($k_3{}^{Quino}$)

temperature (K)	$k_1{}'^{Quino}$ (M^{-1} s^{-1})	$k_3{}^{Quino}$ (M^{-1} s^{-1})
243.15	$3.7 \pm 0.3 \times 10^{1}$	$1.49 \pm 0.78 \times 10^{-2}$
253.15	$4.78 \pm 0.08 \times 10^{1}$	$2.07 \pm 0.26 \times 10^{-2}$
263.15	$5.42 \pm 0.06 \times 10^{1}$	$3.01 \pm 0.13 \times 10^{-2}$
273.15	$6.3 \pm 0.2 \times 10^{1}$	$3.33 \pm 0.11 \times 10^{-2}$
$\Delta H^{\ddagger}$ (kJ mol^{-1})	7.8(9)	13(1)
$\Delta S^{\ddagger}$ (J mol^{-1} K^{-1})	−182(3)	−220(4)
E_a (kJ mol^{-1})	10(1)	15(1)

nonzero, and increasing value of the, *y*-intercept with temperature in Figure S4, indicates that either peroxo $\mathbf{3}^{\mathbf{Quino}}$ formation (eq 1), or a step prior to peroxo formation, is reversible. The final absorbance values associated with the maximum accumulation of $\mathbf{6}^{\mathbf{Quino}}$ were found to be independent of $[O_2]$, providing support for irreversible formation of peroxo $\mathbf{3}^{\mathbf{Quino}}$. Together these suggest that a step prior to peroxo $\mathbf{3}^{\mathbf{Quino}}$ formation, i.e., O_2 binding, is reversible (vide infra). The observed pseudo-first-order rate constants, $k_{3,obs}{}^{Quino}$, for eq 2 were found to be independent of $[O_2]$ over the temperature range examined (Figure S5) indicating that the rate of $\mathbf{3}^{\mathbf{Quino}}$ to $\mathbf{6}^{\mathbf{Quino}}$ conversion is zero-order with respect to $[O_2]$.

$$2Mn^{II}(\mathbf{1}^{\mathbf{Quino}}) + O_2 \xrightarrow[k_{1,obs}{}'^{Quino}]{} Mn^{III}{-}O_2{-}Mn^{III}(\mathbf{3}^{\mathbf{Quino}}) \quad (1)$$

$$Mn^{III}{-}O_2{-}Mn^{III}(\mathbf{3}^{\mathbf{Quino}}) \xrightarrow[k_{3,obs}{}^{Quino}]{2H^{\bullet}} Mn^{III}{-}O{-}Mn^{III}(\mathbf{6}^{\mathbf{Quino}}) + H_2O \quad (2)$$

$$\text{rate} = ae^{-k_{1,obs}{}'^{Quino}t} + be^{-k_{3,obs}{}^{Quino}t} \quad (3)$$

In the next set of stopped-flow experiments, the concentration of $\mathbf{1}^{\mathbf{Quino}}$ was varied (0.2−0.8 mM after mixing) while maintaining a fixed excess concentration of O_2 (4.1 mM after mixing) at −10 °C, allowing us to verify the proposed mechanism, and determine the reaction order with respect to Mn^{II} $\mathbf{1}^{\mathbf{Quino}}$. The observed rate constants ($k_{1,obs}{}^{Quino}$ and $k_{3,obs}{}^{Quino}$) were obtained by fitting kinetic traces to eq 3. The observed pseudo-first-order rate constant for the formation of $\mathbf{3}^{\mathbf{Quino}}$ ($k_{1,obs}{}^{Quino}$) displays a linear dependence on the concentration of $\mathbf{1}^{\mathbf{Quino}}$ in the presence of excess $[O_2]$ (Figure S6), confirming second-order dependence on Mn^{II} overall. This would be consistent with $\mathbf{3}^{\mathbf{Quino}}$ being a binuclear peroxo (Figures 3 and S1). A large nonzero intercept (Figure S6) indicates that a process that is first order in Mn^{II} (e.g., eq 4) contributes to the rate-determining step. Observed rate constants, $k_{3,obs}{}^{Quino}$, for the conversion of peroxo $\mathbf{3}^{\mathbf{Quino}}$ to oxo-bridged $\mathbf{6}^{\mathbf{Quino}}$, in the presence of excess $[O_2]$, are independent of $[\mathbf{1}^{\mathbf{Quino}}]$ indicating that this step (eq 6) is zero-order with respect to Mn (Figure S7). Collectively, the O_2 and Mn^{II} concentration-dependence experiments described above are consistent with the proposed stepwise mechanism, outlined in eqs 4−6 above. This reaction sequence is analogous to that previously established for the reaction between Mn^{II} $\mathbf{1}^{\mathbf{Mepy}}$ and O_2. Although not directly observed spectrophotometrically, superoxo $[Mn(L^{Quino})(O_2)]^+$ ($\mathbf{2}^{\mathbf{Quino}}$) is proposed to form as a transient intermediate (eq 4), prior to the formation of the observable peroxo intermediate $\mathbf{3}^{\mathbf{Quino}}$ (eq 5). The analogous 6-Me-pyridine superoxo $\mathbf{2}^{\mathbf{Mepy}}$ (Figure 1) is, in contrast, observed by transient absorption spectroscopy using a stopped-flow instrument.[6] The rate laws for each step in the mechanism are provided in eqs 7−9 below. The first two rate laws, eqs 7 and 8, are analogous to that previously established for $[Mn^{II}(L^{Mepy})]^+$ ($\mathbf{1}^{\mathbf{Mepy}}$, Figure 1).[6] Information regarding the rate of peroxo O−O bond cleavage was not available for the 6-Me-pyridine system, however, because this step was too slow.[6]

$$Mn^{II}(\mathbf{1}^{\mathbf{Quino}}) + O_2 \xrightarrow[k_1{}^{Quino}]{} Mn^{III}{-}O_2(\mathbf{2}^{\mathbf{Quino}}) \quad (4)$$

Table 3. Calculated Rate Constants, Obtained from Global Fits to Time-Resolved Spectra, and Activation Parameters for the Formation of Putative Superoxo $\mathbf{2}^{\mathbf{Quino}}$ ($k_{1,calc}{}^{Quino}$), Peroxo-Bridged $\mathbf{3}^{\mathbf{Quino}}$ ($k_{2,calc}{}^{Quino}$), and Oxo-Bridged $\mathbf{6}^{\mathbf{Quino}}$ ($k_{3,calc}{}^{Quino}$) in the Reaction between $\mathbf{1}^{\mathbf{Quino}}$ and O_2 in CH_3CN

temperature (K)	$k_{1,calc}{}^{Quino}$ (M^{-1} s^{-1})	$k_{2,calc}{}^{Quino}$ (M^{-1} s^{-1})	$k_{3,calc}{}^{Quino}$ (s^{-1})
243.15	$1.79 \pm 0.05 \times 10^{1}$	$8.80 \pm 0.05 \times 10^{3}$	$1.54 \pm 0.16 \times 10^{-2}$
253.15	$2.24 \pm 0.01 \times 10^{1}$	$1.30 \pm 0.20 \times 10^{4}$	$2.31 \pm 0.12 \times 10^{-2}$
263.15	$3.00 \pm 0.08 \times 10^{1}$	$1.59 \pm 0.06 \times 10^{4}$	$3.07 \pm 0.30 \times 10^{-2}$
273.15	$4.98 \pm 0.09 \times 10^{1}$	$2.30 \pm 0.30 \times 10^{4}$	$3.12 \pm 0.25 \times 10^{-2}$
$\Delta H^{\ddagger}$ (kJ mol^{-1})	16(3)	15(6)	16(2)
$\Delta S^{\ddagger}$ (J mol K^{-1})	−150(12)	−106(5)	−211(6)
E_a (kJ mol^{-1})	18(3)	17(5)	18(3)

DOI: 10.1021/jacs.9b04729
J. Am. Chem. Soc. 2019, 141, 15046−15057

$$Mn^{III}{-}O_2(\mathbf{2}^{Quino}) + Mn^{II}(\mathbf{1}^{Quino}) \xrightarrow[k_2^{Quino}]{} Mn^{III}{-}O_2{-}Mn^{III}(\mathbf{3}^{Quino}) \quad (5)$$

$$Mn^{III}{-}O_2{-}Mn^{III}(\mathbf{3}^{Quino}) \xrightarrow[k_3^{Quino}]{2H^{\bullet}} {+}Mn^{III}{-}O{-}Mn^{III}(\mathbf{6}^{Quino}) + H_2O \quad (6)$$

$$rate_1 = k_1^{Quino}[Mn^{II}(\mathbf{1}^{Quino})][O_2] \quad (7)$$

$$rate_2 = k_2^{Quino}[Mn{-}O_2(\mathbf{2}^{Quino})][Mn^{II}(\mathbf{1}^{Quino})] \quad (8)$$

$$rate_3 = k_3^{Quino}[Mn^{III}{-}O_2{-}Mn^{III}(\mathbf{3}^{Quino})] \quad (9)$$

The proposed mechanism for the formation of quino peroxo $\mathbf{3}^{Quino}$ and its conversion to mono oxo-bridged $\mathbf{6}^{Quino}$ (Scheme 1), summarized in eqs 4–6, was verified using global fits to the time-resolved spectra using ReactLab. The rate constants ($k_{1,calc}{}^{Quino}$, $k_{3,calc}{}^{Quino}$) obtained from these global fits (Table 3) show that the rate at which O_2 binds to $\mathbf{1}^{Quino}$ ($k_{1,calc}{}^{Quino}$, Table 3) is roughly equivalent to the rate at which peroxo $\mathbf{3}^{Quino}$ is observed to form ($k_1{}'^{Quino}$, Table 2, Figure 4). In other words,

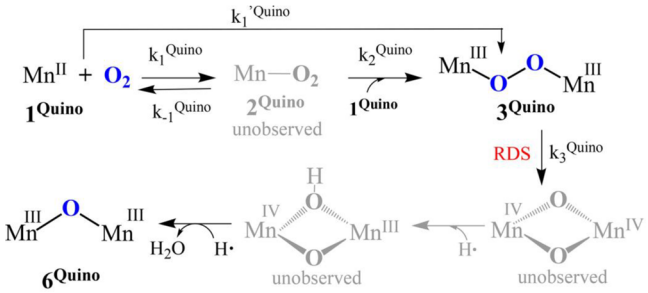

Figure 4. Dioxygen reactivity of Mn^{II} $\mathbf{1}^{Quino}$, showing rate constant labeling scheme, as well as observed versus unobserved intermediates.

the rate-determining step in peroxo $\mathbf{3}^{Quino}$ formation involves O_2 binding. Consistent with this, the rate at which superoxo $\mathbf{2}^{Quino}$ converts to peroxo $\mathbf{3}^{Quino}$ ($k_2{}^{Quino}$) is 2 orders of magnitude faster (Table 3) than the rate at which it forms ($k_1{}^{Quino}$), making it impossible to observe (Figure 4). Calculated spectra (Figure S8) are in good agreement with the experimentally measured spectrum (Figure 2).[48] A comparison with our previously reported system,[6] shows that the rate at which O_2 binds to $\mathbf{1}^{Quino}$ (30.0(8) M^{-1} s^{-1}, Table 3) is 2 orders of magnitude slower than the rate at which O_2 binds to $\mathbf{1}^{Mepy}$ ($3.8(2) \times 10^3$ M^{-1} s^{-1}), at 263 K. The rate at which superoxo $\mathbf{2}^{Quino}$ converts to peroxo $\mathbf{3}^{Quino}$ ($1.6(6) \times 10^4$ M^{-1} s^{-1}, Table 3), on the other hand, is 2 orders of magnitude faster (at 263 K) than the conversion (Figure 1) of superoxo $\mathbf{2}^{Mepy}$ to peroxo $\mathbf{3}^{Mepy}$ ($k_2{}^{Mepy} = 4.17(3) \times 10^2$ M^{-1} s^{-1}).[6] It is worth noting that the rate constant $k_2{}^{Quino}$ is less reliable than $k_3{}^{Quino}$, since it was calculated using global fits. The nonzero, and increasing value of the *y*-intercept with temperature in the $k_{1,obs}{}'^{Quino}$ versus [O_2] plots of Figure S4 indicates that the rate-determining step, i.e., O_2 binding to $\mathbf{1}^{Quino}$, is reversible. One can obtain the rate constant associated with the release of O_2 from the intercept of these plots, and then calculate the temperature-dependent equilibrium constants, $K_{eq}{}^{Quino} = k_1{}^{Quino}/k_{-1}{}^{Quino}$, summarized in Table 4. Previously reported superoxo $\mathbf{2}^{Mepy}$, on the other hand, does not release O_2 once it binds.[6] Thermodynamic parameters for O_2 binding to $\mathbf{1}^{Quino}$ ($\Delta H = -20$ kJ mol^{-1} and $\Delta S = -23$ J mol^{-1} K^{-1}) were

Table 4. Temperature-Dependent Rate-Constant for O_2 Release from $\mathbf{2}^{Quino}$, and Temperature-Dependent Equilibrium Constant for Reversible O_2 Binding to $\mathbf{1}^{Quino}$

temperature (K)	$k_{-1}{}^{Quino}$ (s^{-1})	$K_{eq}{}^{Quino}$ (M^{-1})
273.15	9.8×10^{-2}	640
263.15	6.1×10^{-2}	890
253.15	3.3×10^{-2}	1500
243.15	1.9×10^{-2}	1900

obtained from a van't Hoff plot (Figure S9). The negative entropy value is consistent with an associative process. The activation parameters for O_2 release from $\mathbf{2}^{Quino}$, $E_a = 30(5)$ kJ mol^{-1}, $\Delta H^{\ddagger} = 28(3)$, and $\Delta S^{\ddagger} = -160(9)$, were obtained from Arrhenius (Figure S10) and Eyring (Figure S11) plots, respectively. Although the negative entropy of activation is not what one would expect for a dissociative process, it indicates that the barrier associated with the bond rearrangement required for electron transfer ($Mn^{III} \rightarrow Mn^{II}$) is large enough to offset the entropy gained via O_2 release. The K_{eq} for O_2 binding to $\mathbf{1}^{Quino}$ is 4 orders of magnitude larger than K_{eq} for O_2 binding to [(py)Mn^{II}(TPP)] (K_{eq}(298 K) = 2.3×10^{-2} M^{-1}),[41] but comparable to K_{eq} for O_2 binding to [Co^{II}(SalMeDPT))] (**7**, K_{eq}(233 K) = 1.63×10^3 M^{-1}).[50] The kinetic barrier to O_2 binding, $\Delta H^{\ddagger}$, is 3.4 kJ mol^{-1} higher than that of **7**,[50] but 7 kJ mol^{-1} lower than O_2 binding to MbFe(II) (Mb = myoglobin).[51] The barrier to O_2 release is 13 kJ mol^{-1} higher than that of **7**-O_2,[50] and 9 kJ mol^{-1} higher than that of MbFe-O_2.[51]

Activation parameters (Tables 2 and 3) for peroxo $\mathbf{3}^{Quino}$ formation (Figure S12 and S13), O_2 binding to $\mathbf{1}^{Quino}$ (Figure S14 and S15), as well as superoxo $\mathbf{2}^{Quino}$→ peroxo $\mathbf{3}^{Quino}$ conversion (Figure S16 and S17), were obtained from Eyring and Arrhenius plots. The largest errors are associated with the conversion of superoxo $\mathbf{2}^{Quino}$ to peroxo $\mathbf{3}^{Quino}$, since the superoxo intermediate is not directly observed. The enthalpy of activation ($\Delta H_1{}^{\ddagger Mepy}$) associated with O_2 binding to $\mathbf{1}^{Mepy}$ (26(2) kJ/mol)[6] is 1.6 times greater than that for O_2 binding to $\mathbf{1}^{Quino}$ (16(3) kJ/mol, Table 3). A negative entropy of activation ($\Delta S_1{}^{\ddagger Mepy}$, Table 3) is seen with both $\mathbf{1}^{Mepy}$ and $\mathbf{1}^{Quino}$, consistent with an associative process. With the 6-Me-pyridine ligand system, the barrier to the conversion of superoxo $\mathbf{2}^{Mepy}$ to peroxo $\mathbf{3}^{Mepy}$ ($E_a = 49$ kJ mol^{-1}) is significantly higher than the barrier to O_2 binding ($E_a = 26(2)$ kJ mol^{-1}), explaining why the superoxo intermediate is observed. For the quinoline system, both of these barriers are significantly lower ($E_a = 18(3)$ kJ mol^{-1}, Figure S15), and $E_a = 17(5)$ kJ mol^{-1} (Figure S17), respectively), and the reaction landscape is relatively flat, explaining why it is more difficult to trap superoxo $\mathbf{2}^{Quino}$.

The Barrier to Peroxo O–O Bond Cleavage. With the 6-Me-pyridine ligand scaffold, cleavage of the peroxo O–O bond of $\mathbf{3}^{Mepy}$ was determined to be slow and rate-limiting, making it difficult to obtain information regarding the mechanism of $\mathbf{3}^{Mepy}$ to mono oxo-bridged $\mathbf{6}^{Mepy}$ conversion (Figure 1).[6] In contrast, the rate at which the less stable quinoline peroxo, $\mathbf{3}^{Quino}$ converts to mono-oxo bridged $\mathbf{6}^{Quino}$ (Table S5) is an order of magnitude faster (vide infra), allowing us to obtain stopped-flow kinetics data for this step. Calculated rate constants ($k_{3,calc}{}^{Quino}$) obtained from global fits (Table 3) are in good agreement with the experimentally determined rate constants ($k_3{}^{Quino}$, Table 2).

Activation parameters (Table 2) for peroxo O–O bond cleavage were obtained from Eyring and Arrhenius plots (Figure 5 and Figures S18–S20). Although activation parameters are not available for comparison to other Mn-peroxo compounds,

DOI: 10.1021/jacs.9b04729
J. Am. Chem. Soc. 2019, 141, 15046–15057

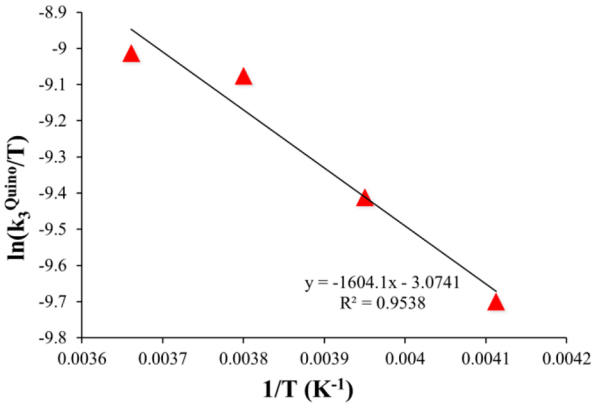

Figure 5. Eyring plot for cleavage of the peroxo O−O bond of $\mathbf{3}^{\mathbf{Quino}}$ and its conversion to mono oxo-bridged $\mathbf{6}^{\mathbf{Quino}}$ in CH_3CN, from which activation parameters $\Delta H_3^{\ddagger Quino}$ = 13(1) kJ mol^{-1} and $\Delta S_3^{\ddagger Quino}$ = −220(4) J mol^{-1} K^{-1}, were obtained. First-order rate constants k_3^{Quino} were obtained from stopped-flow experiments.

the barrier to cleavage of the peroxo O−O bond of $\mathbf{3}^{\mathbf{Quino}}$ is comparable to the barrier to homolytic O−O bond cleavage for Fe hydroperoxo $[(TMC)Fe^{III}–OOH]^{2+}$.[52]

If Mn peroxo $\mathbf{3}^{\mathbf{Quino}}$ follows a pathway (Figure 4) analogous to that of Cu- and Fe-peroxo compounds,[13−19] then homolytic O−O bond cleavage would afford a high-valent bis-oxo-bridged compound, $L^{Quino}Mn^{IV}(\mu\text{-}O)_2Mn^{IV}L^{Quino}$ ($\mathbf{4}^{\mathbf{Quino}}$). Two electrons, and two protons, or, two H atoms, would then be required to convert this high-valent bis-oxo intermediate to mono-oxo bridged $L^{Quino}Mn^{III}{}_2(\mu\text{-}O)$ ($\mathbf{6}^{\mathbf{Quino}}$). We were unable to observe intermediates following quinoline peroxo $\mathbf{3}^{\mathbf{Quino}}$, however, even at temperatures as low as −120 °C (in Me-THF). This implies that O−O bond cleavage is the rate-determining step in this case. In order to increase the stability of high-valent intermediates and increase the likelihood of observing intermediates beyond the peroxo, we synthesized a more electron-rich ligand system, containing a 6-MeO-pyridine substituent, L^{MeOpy}.

Synthesis of a New Mn^{II} Complex Containing a Less Sterically Encumbered, More Electron-Donating Pyridine Substituent. The pentadentate ligand L^{MeOpy}, which is a derivative of previously reported L^{MePy}, was synthesized according to the procedure outlined in the Supporting Information. This ligand features a 6-methoxy-pyridine substituent, which is simultaneously more electron-donating and less sterically encumbering than L^{MePy} (A-value = 0.6 versus 1.7 for MeO and Me, respectively).[53] The corresponding Mn^{II} complex, $[Mn^{II}(L^{MeOpy})]_2^{2+}$ ($\mathbf{1}^{\mathbf{MeOpy}}$), was synthesized via a metal-templated Schiff-base condensation between *N*,*N*-bis(6-methoxy-2-pyridilmethyl)ethane-1,2-diamine and 3-methyl-3-mercapto-2-butanone, as previously described for $\mathbf{1}^{\mathbf{Mepy}}$ and $\mathbf{1}^{\mathbf{Quino}}$.[48] Crystallographic characterization showed that the Mn^{II} complex derived from this ligand, $\mathbf{1}^{\mathbf{MeOpy}}$, is dimeric in the solid state (Figure S21). However, its magnetic moment (μ_{eff} = 5.88 μ_B, CH_3CN, 298 K), EPR spectrum (hyperfine splitting 90 G, Figure S22), and solution-state ESI-MS (Figure S23), and cyclic voltammogram (Figure S24) all indicate that it is monomeric in solution.

Reactivity of $\mathbf{1}^{\mathbf{MeOpy}}$ with Dioxygen. Like complexes $\mathbf{1}^{\mathbf{Mepy}}$ and $\mathbf{1}^{\mathbf{Quino}}$, reduced $\mathbf{1}^{\mathbf{MeOpy}}$ rapidly reacts with O_2 (Scheme 1) under ambient conditions to ultimately afford binuclear mono oxo-bridged $\{[Mn^{III}(L^{MeOpy})]_2(\mu\text{-}O)\}^{2+}$ ($\mathbf{6}^{\mathbf{MeOpy}}$), characterized by its λ_{max} = 565 nm (ε = 1030 M^{-1} cm^{-1}) in the electronic absorption spectrum (Figure S25), the ORTEP of which is shown in Figure 6. The mean Mn···N^{Ar} separation in $\mathbf{6}^{\mathbf{MeOpy}}$ is

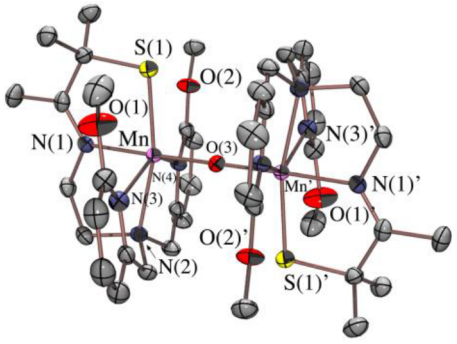

Figure 6. ORTEP diagram of mono oxo bridged $\mathbf{6}^{\mathbf{MeOpy}}$ formed in the reaction between $\mathbf{1}^{\mathbf{MeOpy}}$ and O_2. Hydrogens have been omitted for clarity.

0.15 Å shorter than that of 6-Me-pyridine $\mathbf{6}^{\mathbf{Mepy}}$, and 0.18 Å longer than that of 6-H-pyridine $\mathbf{6}^{\mathbf{py}}$ (Table 1), indicating, based on previously established trends,[54] that the corresponding peroxo derivative should have a weaker O−O bond, but will likely be observable (vide supra). In addition, the more electron-rich metal ion should be capable of stabilizing high-valent intermediates (vide infra). Consistent with this, four metastable intermediates are observed en route to mono oxo-bridged $\mathbf{6}^{\mathbf{MeOpy}}$. At low temperatures (−73 °C) a metastable green intermediate, $\mathbf{3}^{\mathbf{MeOpy}}$, ($\lambda_{max}(CH_3CH_2CN)$ = 612 nm, $\lambda_{max}(CH_2Cl_2)$ = 630 nm) is observed in the reaction between $\mathbf{1}^{\mathbf{MeOpy}}$ and O_2 (Figure 7). Given the similarity of this spectrum

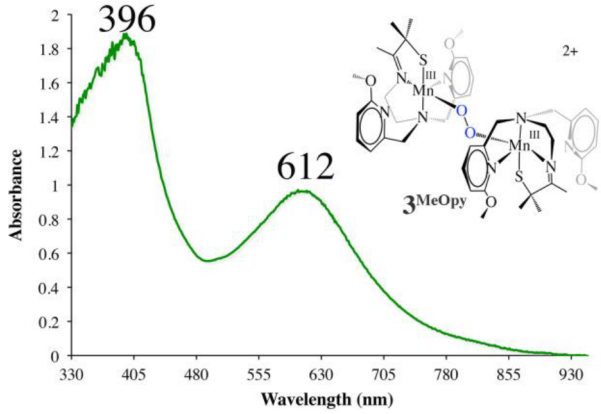

Figure 7. Electronic absorption spectrum of peroxo intermediate $\mathbf{3}^{\mathbf{MeOpy}}$ formed in the reaction between $\mathbf{1}^{\mathbf{MeOpy}}$ and O_2 (5 mL dry O_2 gas) in CH_3CH_2CN at −73 °C.

(Figure 7) to that of peroxo-bridged $\mathbf{3}^{\mathbf{Mepy}}$ (λ_{max} = 640 nm, Figure 2)[6] and peroxo-bridged $\mathbf{3}^{\mathbf{Quino}}$ (λ_{max} = 660 nm, Figure 2), this intermediate was tentatively assigned as a peroxo-bridged dimer, $\{[Mn^{III}(L^{MeOpy})]_2(\mu\text{-}O_2)\}^{2+}$($\mathbf{3}^{\mathbf{MeOpy}}$). DFT and TD-DFT calculations were found to support this assignment. Metrical parameters (Table S6) for the DFT optimized structure, calculated using the spin-unrestricted B3LYP hybrid functional and the 6-311G basis set, are consistent with $\mathbf{3}^{\mathbf{MeOpy}}$ being a *trans*-μ-1,2-peroxo-bridged Mn^{III} dimer (Figure 8), analogous to $\mathbf{3}^{\mathbf{Mepy}}$ and $\mathbf{3}^{\mathbf{Quino}}$. The TD-DFT calculated electronic absorption spectrum (Figure S26) is in good agreement with the experimental spectrum of Figure 7, and

DOI: 10.1021/jacs.9b04729
J. Am. Chem. Soc. 2019, 141, 15046−15057

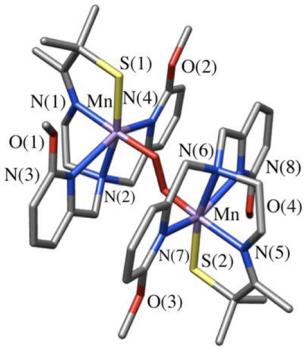

Figure 8. DFT optimized structure of peroxo-bridged $\mathbf{3}^{\mathbf{MeOpy}}$. O−O = 1.518 Å, Mn−$O_{avg}$ = 1.86 Å, Mn−S_{avg} = 2.33; Mn(1)···Mn(2) = 4.361 Å, Mn−O−O_{avg} = 106°.

the calculated exchange coupling constant, J^{calc} = −0.53 cm^{-1}, indicates that the two Mn^{III} ions are essentially uncoupled. The calculated O−O bond length (1.518 Å) is 0.02 Å longer than that of $\mathbf{3}^{\mathbf{Quino}}$, and 0.07 Å longer than that of $\mathbf{3}^{\mathbf{Mepy}}$ (O−O = 1.452(5) Å),[6] indicating that this bond should cleave more readily in $\mathbf{3}^{\mathbf{MeOpy}}$. Consistent with this, $\mathbf{3}^{\mathbf{MeOpy}}$ is less stable than $\mathbf{3}^{\mathbf{Mepy}}$ and $\mathbf{3}^{\mathbf{Quino}}$, and is not readily observed at temperatures above −73 °C unless a stopped-flow instrument is used.

Kinetics data for O_2 binding to Mn^{II} $\mathbf{1}^{\mathbf{MeOpy}}$ and the formation of putative peroxo $\mathbf{3}^{\mathbf{MeOpy}}$ were collected at low temperatures using a stopped-flow instrument. The build-up and decay of putative superoxo $\mathbf{2}^{\mathbf{MeOpy}}$ was followed at 504 nm. As illustrated in the time-resolved electronic absorption spectra of Figure 9,

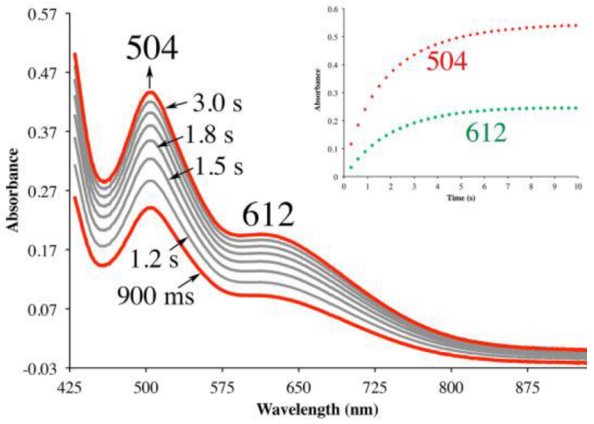

Figure 9. Time-resolved electronic absorption spectra, for dioxygen binding to $\mathbf{1}^{\mathbf{MeOpy}}$ in CH_3CH_2CN at −80 °C, obtained using a stopped-flow instrument, under pseudo-first-order conditions with excess O_2 ([$\mathbf{1}^{\mathbf{MeOpy}}$] = 0.375 mM, [$O_2$] = 8 mM after mixing). Inset: kinetic trace obtained at λ_{max} = 504 and 612 nm.

$\mathbf{2}^{\mathbf{MeOpy}}$ forms in approximately 3 s at −80 °C, en route to putative peroxo $\mathbf{3}^{\mathbf{MeOpy}}$ (λ_{max} = 612 nm). The electronic absorption spectrum of $\mathbf{2}^{\mathbf{MeOpy}}$ is similar to that of our previously reported superoxo, $\mathbf{2}^{\mathbf{Mepy}}$ (Figure 1, λ_{max} = 515 nm),[6] which forms en route to crystallographically characterized $\mathbf{3}^{\mathbf{Mepy}}$, suggesting that $\mathbf{2}^{\mathbf{MeOpy}}$ is a superoxo, $[Mn(L^{MeOpy})(O_2)]^+$ ($\mathbf{2}^{\mathbf{MeOpy}}$). In contrast to $\mathbf{2}^{\mathbf{Mepy}}$, however, $\mathbf{2}^{\mathbf{MeOpy}}$ is only cleanly observed if ≥20-fold excess [O_2] (8 mM [O_2] vs 0.375 mM [$\mathbf{1}^{\mathbf{MeOpy}}$]) and lower temperatures (−80 °C to −62 °C) are used (Table S7, Figure S27). These conditions are likely required in order to ensure that Mn^{II} $\mathbf{1}^{\mathbf{MeOpy}}$ is consumed by the excess O_2, thereby slowing down the conversion of $\mathbf{2}^{\mathbf{MeOpy}}$ to binuclear peroxo-bridged $\mathbf{3}^{\mathbf{MeOpy}}$ (Figures 10 and S27) and increasing its lifetime. The general kinetic scheme used to analyze the data was the same as that used for $\mathbf{1}^{\mathbf{Mepy}}$.[6] Reactions were run under pseudo-first-order conditions, in the presence of excess O_2. Pseudo-first-order rate constants, $k_{1,obs}^{MeOpy}$ and $k_{2,obs}^{MeOpy}$, as a function of [O_2], temperature, and [$\mathbf{1}^{\mathbf{MeOpy}}$] are assembled in Tables S7–S9, respectively. The observed rate constant $k_{1,obs}^{MeOpy}$ was found to increase linearly (Figure S28) with increasing O_2 concentration, indicative of a first order reaction with respect to [O_2]. The second order rate constant for O_2 binding k_1^{MeOpy} was obtained from the slope, and the first order rate constant for O_2 release at −80 °C, k_{-1}^{MeOpy}, was obtained from the intercept of Figure S28. Intermediates $\mathbf{2}^{\mathbf{MeOpy}}$ and $\mathbf{3}^{\mathbf{MeOpy}}$ were found to be too unstable at temperatures above −80 °C if lower concentrations of dioxygen (i.e., [O_2] < 8.8 mM) are used, requiring that, at higher temperatures, k_{-1}^{MeOpy} parameters be obtained from Global fits. Second order rate constants for the conversion of superoxo $\mathbf{2}^{\mathbf{MeOpy}}$ to peroxo $\mathbf{3}^{\mathbf{MeOpy}}$, k_2^{MeOpy}, were also obtained from Global fits to the ([O_2] = 8.8 mM) data using ReactLab. Superoxo $\mathbf{2}^{\mathbf{MeOpy}}$ is not observed at temperatures above −62 °C.

Temperature-dependent rate constants for the reaction between $\mathbf{1}^{\mathbf{MeOpy}}$ and O_2 (Scheme 1) are summarized in Tables S7–S8, and Tables S11–S12. The rate constant numbering scheme and observed intermediates are shown in Figure 10. Dioxygen binding to $\mathbf{1}^{\mathbf{MeOpy}}$ (k_1^{MeOpy}(211 K) = 70.9(8) M^{-1} s^{-1}, Table S9, Figure S28) is 2 orders of magnitude slower than O_2 binding to $\mathbf{1}^{\mathbf{Mepy}}$ (k_1^{Mepy}(263 K) = 3.8(2) × 10^3 M^{-1} s^{-1}),[6] and approximately twice as fast as O_2 binding to $\mathbf{1}^{\mathbf{Quino}}$ ($k_{1,calc}^{Quino}$(263 K) = 30.0(8) M^{-1} s^{-1}, Table 3), albeit at lower temperatures, where entropy favors an associative binding process. This step is rate determining, with respect to formation of peroxo $\mathbf{3}^{\mathbf{Quino}}$ and $\mathbf{3}^{\mathbf{MeOpy}}$, but not $\mathbf{3}^{\mathbf{Mepy}}$. Dioxygen binds reversibly to $\mathbf{1}^{\mathbf{MeOpy}}$, as well as $\mathbf{1}^{\mathbf{Quino}}$ (vide supra), but irreversibly to $\mathbf{1}^{\mathbf{Mepy}}$. Dioxygen release from $\mathbf{2}^{\mathbf{MeOpy}}$ is 3 orders of magnitude slower (k_{-1}^{MeOpy} = 2.4(2) × 10^{-2} s^{-1}, Table S10) than O_2 binding (k_1^{MeOpy} = 70.9(8) M^{-1} s^{-1}) at −80 C. Due to the instability of superoxo $\mathbf{2}^{\mathbf{MeOpy}}$ at temperatures above −80 °C, and the limitations of the low-temperature stopped-flow instrument, the error associated with the kinetic parameters, k_{-1}^{MeOpy}, for O_2 release is too large to reasonably obtain equilibrium constants. The apparent low affinity for O_2 (based on the intercept of Figure S28), and the reversibility of O_2 binding to $\mathbf{1}^{\mathbf{MeOpy}}$ indicates that, consistent with our design, the electron donating L^{MeOpy} ligand decreases the metal ion Lewis acidity of the 6-MeO-pyridine dioxygen derivatives. This is reflected in the $Mn^{II/III}$ redox potentials for $\mathbf{1}^{\mathbf{MeOpy}}$ versus $\mathbf{1}^{\mathbf{Quino}}$ and $\mathbf{1}^{\mathbf{Mepy}}$ (vide infra). This is not only an electronic effect, but also a steric effect since the decreased steric bulk of the 6-MeO-pyridine substituent favors shorter Mn···N^{Ar} distances, which should increase electron density at the metal ion (vide supra, Table 1).[11,49]

Eyring and Arrhenius plots were used to obtain activation parameters for O_2 binding to $\mathbf{1}^{\mathbf{MeOpy}}$ (Figures S29–S30), O_2 release from $\mathbf{2}^{\mathbf{MeOpy}}$ (Figures S31–S32), and the conversion of superoxo $\mathbf{2}^{\mathbf{MeOpy}}$ to peroxo $\mathbf{3}^{\mathbf{MeOpy}}$ (Figures S33–S34), and are compared with the corresponding parameters for $\mathbf{1}^{\mathbf{Mepy}}$ and $\mathbf{1}^{\mathbf{Quino}}$ in Table S10. An analysis of the factors that govern the magnitude of these kinetic barriers shows that both metal ion Lewis acidity and metal ion accessibility play a role. For example, there is a strong correlation (R^2 = 0.999) between the barrier to O_2 binding and the cathodic peak potential, $E_{p,c}$,[48] an experimental parameter that reflects metal ion Lewis acidity:

DOI: 10.1021/jacs.9b04729
J. Am. Chem. Soc. 2019, 141, 15046−15057

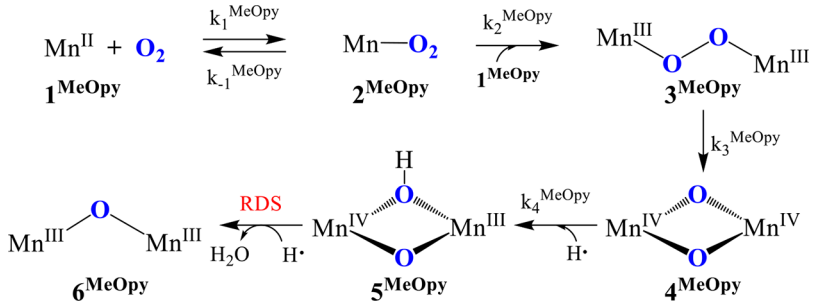

Figure 10. Dioxygen reactivity of 6-MeO-pyridine $\mathbf{1}^{\mathbf{MeOpy}}$, showing rate constant labeling scheme, and observed intermediates.

the higher the redox potential, the higher the barrier to O_2 binding (Figure 11). This indicates O_2 binding is coupled with

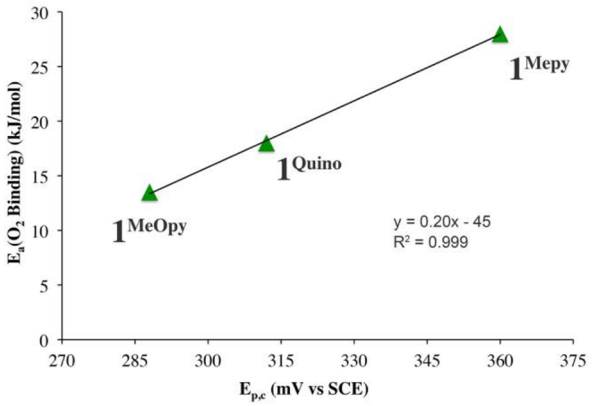

Figure 11. Correlation between the activation barrier (E_a) to O_2 binding and the cathodic peak potential, $E_{p,c}$.

the oxidation of the metal ion, as one would expect for a process that converts O_2 to superoxide, $O_2^{\bullet-}$. Peak potentials, as opposed to $E_{1/2}$ values are compared in Figure 11, since the cyclic voltammogram wave associated with the $\mathbf{1}^{\mathbf{Quino}}$ is irreversible.[55] In addition, comparison of the steric properties shows that the activation barrier decreases as the metal ion becomes more accessible (Figures 12, 13, and S34). The Mn(II)

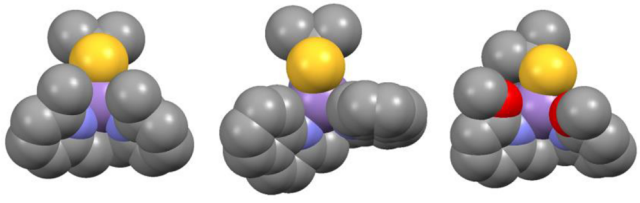

Figure 12. Steric properties of the ligand influence metal ion (shown in purple) accessibility, as shown by space filling diagrams of $\mathbf{1}^{\mathbf{Mepy}}$ (left), $\mathbf{1}^{\mathbf{Quino}}$ (center), and $\mathbf{1}^{\mathbf{MeOpy}}$ (right).

ion is more accessible in $\mathbf{1}^{\mathbf{MeOpy}}$, less so in $\mathbf{1}^{\mathbf{Quino}}$, and least accessible in the more sterically encumbered $\mathbf{1}^{\mathbf{Mepy}}$. A similar correlation is observed between the redox potential and the kinetic barrier to the conversion of superoxo **2** to the corresponding peroxo **3** (Figure 13).

Barrier to O−O Bond Cleavage and the Observation of Additional Intermediates. As noted in the introduction, the steric properties of the substituted N-heterocycles differ dramatically, and have been shown to influence the barrier to alkylperoxo O−O bond cleavage.[6] The least sterically

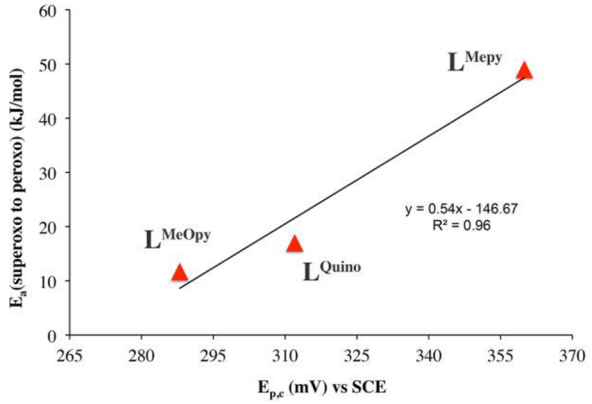

Figure 13. Correlation between cathodic peak potential, $E_{p,c}$, and the kinetic barrier to the conversion of superoxo **2** to peroxo **3**.

encumbered complexes contain shorter Mn···N^{Ar} distances and weaker alkylperoxo O−O bonds. This is because the metal ion becomes less Lewis acidic as the Mn···N^{Ar} distance decreases, and this decreases π-interaction between the peroxo π^*(O−O) orbital and the metal ion d-orbital the filled peroxo π^*(O−O) orbital to the metal ion. X-ray emission (XES) spectroscopically calibrated calculations showed that peroxo $\mathbf{3}^{\mathbf{Mepy}}$ adheres to this correlation, as well.[11] Presumably this also applies to the other dioxygen-derived peroxos, $\mathbf{3}^{\mathbf{Quino}}$ and $\mathbf{3}^{\mathbf{MeOpy}}$, described herein (Scheme 1). Kinetic studies were used to determine whether this was indeed the case.

Observation of peroxo $\mathbf{3}^{\mathbf{MeOpy}}$, and the metastable intermediates that follow, is optimized when excess amounts of O_2 ($[O_2]$ = 8.8 mM vs $[\mathbf{1}^{\mathbf{MeOpy}}]$ = 0.375 mM) and higher temperatures (−44 °C), are used (Figure 14). These conditions speed up the formation of superoxo $\mathbf{2}^{\mathbf{MeOpy}}$ and its conversion to peroxo $\mathbf{3}^{\mathbf{MeOpy}}$. Under these conditions, peroxo $\mathbf{3}^{\mathbf{MeOpy}}$ forms within 1.2 s (Figure 14), and then converts within 21 s to a metastable species, $\mathbf{4}^{\mathbf{MeOpy}}$. There is a clean isosbestic point at 730 nm, indicating that at most two species contribute to the absorbance at higher wavelengths. However, at wavelengths below 525 nm, the isosbestic points are less clear because several species (including superoxo $\mathbf{2}^{\mathbf{MeOpy}}$, and peroxo $\mathbf{3}^{\mathbf{MeOpy}}$) contribute to this region of the spectrum. On the basis of global fits to the data, $\mathbf{4}^{\mathbf{MeOpy}}$ possesses absorption bands at 805 and 497 nm, and a shoulder at 532 nm (Figure 14).

According to the reaction scheme of Figure 10, the species most likely to form following peroxo $\mathbf{3}^{\mathbf{MeOpy}}$, would be a high-valent bis μ-oxo, $[((L^{MeOpy})Mn^{IV})_2(\mu^2\text{-}O)_2]^{2+}$ ($\mathbf{4}^{\mathbf{MeOpy}}$). Conversion of $\mathbf{3}^{\mathbf{MeOpy}}$ to $\mathbf{4}^{\mathbf{MeOpy}}$ would involve peroxo O−O bond cleavage, explaining why higher temperatures are required. Rate constants for the conversion of $\mathbf{3}^{\mathbf{MeOpy}}$ to $\mathbf{4}^{\mathbf{MeOpy}}$ were obtained

DOI: 10.1021/jacs.9b04729
J. Am. Chem. Soc. 2019, 141, 15046−15057

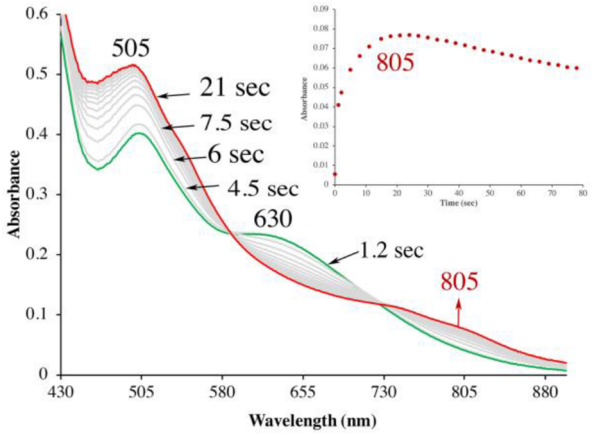

Figure 14. Conversion of peroxo $\mathbf{3}^{\mathbf{MeOpy}}$ to a metastable species, $\mathbf{4}^{\mathbf{MeOpy}}$, with λ_{max} = 805 nm monitored by transient absorption spectroscopy in CH_3CH_2CN at −44 °C. $[O_2]$ = 8.8 mM, $[\mathbf{1}^{\mathbf{MeOpy}}]$ = 0.375 mM, after mixing.

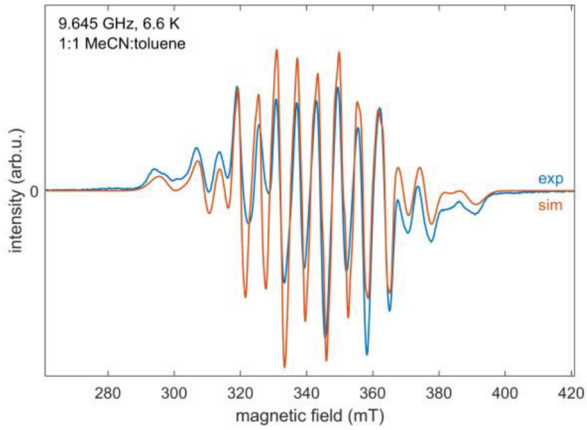

Figure 15. Low temperature (6.6 K) perpendicular-mode X-band (9.645 GHz) EPR spectrum of the Mn(III)Mn(IV) intermediate, **15**, observed following peroxo **12**. Microwave power = 0.2 mW, modulation amplitude = 0.75 mT.

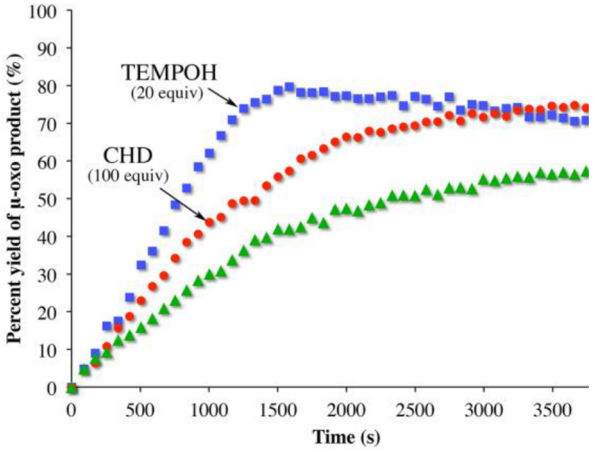

Figure 16. Comparison of the rates of formation and yield of $\mathbf{6}^{\mathbf{MeOpy}}$ in CH_2Cl_2, both in the absence (green) and presence of sacrificial H atom donors CHD (red) or TEMPOH (blue).

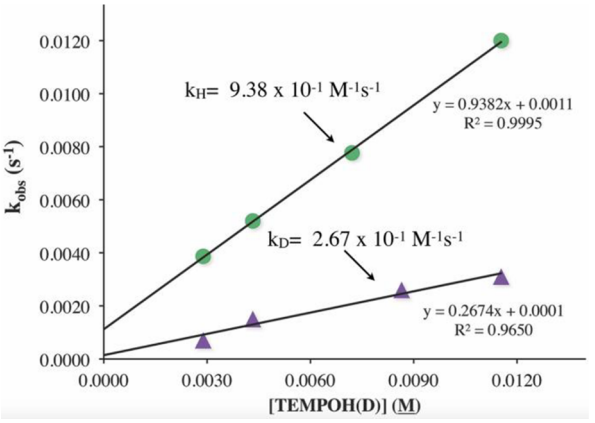

Figure 17. Deuterium isotope effect observed when TEMPOH(D) is used as a sacrificial H atom donor for the conversion of $\mathbf{5}^{\mathbf{MeOpy}}$ to $\mathbf{6}^{\mathbf{MeOpy}}$.

from Global fits to the data. A comparison of the half-lives of $\mathbf{3}^{\mathbf{MeOpy}}$ (k_3^{MeOpy} (193 K) = 0.06(3) s^{-1}, $t_{1/2}$ = 11.5 s), $\mathbf{3}^{\mathbf{Quino}}$ (Table S10), and $\mathbf{3}^{\mathbf{Mepy}}$ (Table S10), shows that there is a correlation between the barrier to peroxo O−O bond cleavage and the experimentally measured redox potential, $E_{p,c}(Mn^{III/II})$. This effect is enhanced if one takes into account the fact that these half-lives were measured at different temperatures, due to the fact that peroxo-bridged $\mathbf{3}^{\mathbf{MeOpy}}$ is not observed above 233 K, and temperatures below 233 K were required for an accurate determination of rate constants for $\mathbf{3}^{\mathbf{Quino}}$ due to its instability. The higher the redox potential, the more Lewis acidic the metal ion, and the more π-interaction with the filled peroxo π^* orbital is facilitated. Redox potentials for the $Mn^{III/II}$ couple are used, as opposed to the $Mn^{IV/III}$ couple, because our Mn(IV) derivatives are too reactive (vide infra) to obtain the latter. The metastable, reactive nature of $\mathbf{4}^{\mathbf{MeOpy}}$ contrasts with the majority of bis-oxo bridged $Mn^{IV}Mn^{IV}$ dimers,[56−58] likely reflecting the electron donating properties of the thiolate.

Following its formation, putative high-valent bis oxo $Mn^{IV}Mn^{IV}$ ($\mathbf{4}^{\mathbf{MeOpy}}$, λ_{max} = 805 nm) converts more slowly (Table S9) to a metastable red species with λ_{max} = 505 nm, and a reproducibly observed multiline ⊥-mode EPR signal (Figure 15). The spectrum of Figure 15 is well simulated with an $S = 1/2$ system with a rhombic **g** tensor with principal values 1.994, 2.004, and 2.016 coupled to two ^{55}Mn nuclei with isotropic hyperfine couplings of 325 and 180 MHz.[59] These values are consistent with an antiferromagnetically coupled $Mn^{III}Mn^{IV}$ dimer.[60−66] If the reaction between $\mathbf{1}^{\mathbf{MeOpy}}$ and O_2 is carried out in the presence of 100 equiv of 1,4-cyclohexadiene (CHD), and then quenched immediately upon the formation of the red, EPR-active intermediate, then 0.5 equiv of benzene is detected by GC−MS (Figure S35). This indicates one H atom is abstracted en route to the red intermediate. If the same reaction is followed to its completion (Figure 10), then 1.0 equiv of benzene is detected, indicating that two H atoms in total, one before, and the other after the red intermediate (Figure S36), are abstracted en route to mono oxo-bridged $\mathbf{6}^{\mathbf{MeOpy}}$. In the absence of a sacrificial H atom donor the yield of $\mathbf{6}^{\mathbf{MeOpy}}$ decreases if it is carried out in CH_2Cl_2 solvent (Figure 16). In this solvent, with its strong C−H bonds (98 kcal/mol), near quantitative yields of $\mathbf{6}^{\mathbf{MeOpy}}$ are only observed when sacrificial H atom donor TEMPOH is added. If TEMPOD is used in place of TEMPOH, then a deuterium isotope effect (k_H/k_D = 3.5) is observed (Figure 17). Together these results indicate that the O_2-promoted conversion of $\mathbf{1}^{\mathbf{MeOpy}}$ to $\mathbf{6}^{\mathbf{MeOpy}}$ requires two e^- and two H^+ (Figure 10).

DOI: 10.1021/jacs.9b04729
J. Am. Chem. Soc. 2019, 141, 15046−15057

CONCLUSIONS

With this study, we have shown that the relative stability of metastable dioxygen intermediates can be tuned by adjusting the supporting ligands. Whereas O_2 binds irreversibly to $\mathbf{1}^{\mathbf{Mepy}}$, kinetics data shows that O_2 binding is less favored for the less Lewis acidic complexes $\mathbf{1}^{\mathbf{Quino}}$ and $\mathbf{1}^{\mathbf{MeOpy}}$, and the microscopic reverse process involving O_2 release from superoxo $\mathbf{2}^{\mathbf{Quino}}$ and $\mathbf{2}^{\mathbf{MeOpy}}$, is more favorable. The Mn^{II} complexes $\mathbf{1}^{\mathbf{Mepy}}$ and $\mathbf{1}^{\mathbf{Quino}}$ are complementary in that the initial O_2 binding step to form a superoxo intermediate is observable with $\mathbf{1}^{\mathbf{Mepy}}$, but not with $\mathbf{1}^{\mathbf{Quino}}$. Information regarding the barrier to peroxo O−O bond cleavage can be obtained for peroxo $\mathbf{3}^{\mathbf{Quino}}$, but not for $\mathbf{3}^{\mathbf{Mepy}}$, or $\mathbf{3}^{\mathbf{MeOpy}}$ because they are too slow or too fast, respectively. The incorporation of a more electron rich, less sterically encumbering ligand (6-MeO-pyridine) ligand decreases the barrier to O_2 binding and release, as well as peroxo O−O bond cleavage, relative to the other derivatives. A strong correlation between the $Mn^{II/III}$ redox potential and the ligand-dependent activation barrier to O_2 binding and the conversion of superoxo **2** to peroxo **3** is observed. The reaction landscape for the dioxygen chemistry of $\mathbf{1}^{\mathbf{Quino}}$ and $\mathbf{1}^{\mathbf{MeOpy}}$ is shown to be relatively flat, compared to that of $\mathbf{1}^{\mathbf{Mepy}}$, with respect to the barriers separating metastable intermediates. With a more electron-donating, less sterically encumbered 6-MeO-pyridine ligand, a total of four intermediates are observed at low temperatures, including two reactive intermediates following peroxo $\mathbf{3}^{\mathbf{MeOpy}}$, en route to the final mono oxo-bridged dimer product, $\mathbf{6}^{\mathbf{MeOpy}}$. Each of the intermediates following the peroxo $\mathbf{3}^{\mathbf{MeOpy}}$ is shown to cleave strong X−H bonds (X = C, O). Two electrons and two protons are shown to be required for the O_2-promoted conversion of Mn^{II} $\mathbf{1}^{\mathbf{MeOpy}}$ to binuclear mono oxo-bridged $\mathbf{6}^{\mathbf{MeOpy}}$. In the absence of a sacrificial H atom donor, such as 1,4-cyclohexadiene (BDE(C−H) = 76.0 kcal/mol) or TEMPOH (BDE(O−H) = 70.6 kcal/mol), this reaction presumably involves the abstraction of H atoms from the C−H bonds (BDE = 94 kcal/mol) of CH_3CH_2CN solvent. With TEMPOH, a deuterium isotope effect is observed (k_H/k_D = 3.5) implicating HAT in each of these steps. The highly reactive nature of putative $Mn^{IV}Mn^{IV}$ contrasts with the majority of $Mn^{IV}Mn^{IV}$ dimers reflecting the electron donor properties of the thiolate ligand.

ASSOCIATED CONTENT

Supporting Information

The Supporting Information is available free of charge on the ACS Publications website at DOI: 10.1021/jacs.9b04729.

Experimental section, crystallographic tables for $\mathbf{1}^{\mathbf{MeOpy}}$, $\mathbf{6}^{\mathbf{MeOpy}}$, and $\mathbf{3}^{\mathbf{Quino}}$; k_{obs} and DFT optimized metrical parameter tables, k_{obs} vs $[O_2]$ or [Mn] plots, van't Hoff plot for O_2 binding to $\mathbf{1}^{\mathbf{MeOpy}}$, Eyring and Arrhenius plots, DFT calculated structures and Mulliken charges, TD-DFT calculated spectra for $\mathbf{3}^{\mathbf{Quino}}$ and $\mathbf{3}^{\mathbf{MeOpy}}$, ORTEP, ESI-MS, and EPR of $\mathbf{1}^{\mathbf{MeOpy}}$, quantitative UV−vis of $\mathbf{6}^{\mathbf{MeOpy}}$ (PDF)

Crystal data (CIF)

Crystal data (CIF)

AUTHOR INFORMATION

Corresponding Author

*kovacs@uw.edu

ORCID

Santiago Toledo: 0000-0002-5096-3396
Ellen C. Hayes: 0000-0001-9081-6131
Marc C. Piquette: 0000-0002-8782-5878
Julian A. Rees: 0000-0003-0883-2680
Stefan Stoll: 0000-0003-4255-9550
Julie A. Kovacs: 0000-0003-2358-1269

Notes

The authors declare no competing financial interest.
†Deceased.

ACKNOWLEDGMENTS

This manuscript is dedicated to the memory of Professor Elena Rybak-Akimova, whose joyful and generous spirit will be with us always. Funding from the NSF (CHE-1664682) is gratefully acknowledged.

REFERENCES

(1) Askerka, M.; Brudvig, G. W.; Batista, V. S. The O2-Evolving Complex of Photosystem II: Recent Insights from Quantum Mechanics/Molecular Mechanics (QM/MM), Extended X-ray Absorption Fine Structure (EXAFS), and Femtosecond X-ray Crystallography Data. *Acc. Chem. Res.* **2017**, *50*, 41−48.

(2) Yano, J.; Yachandra, V. K. Mn4Ca Cluster in Photosynthesis: Where and How Water is Oxidized to Dioxygen. *Chem. Rev.* **2014**, *114*, 4175−4205.

(3) Nocera, D. G. The Artificial Leaf. *Acc. Chem. Res.* **2012**, *45*, 767−776.

(4) Cox, N.; Pantazis, D. A.; Neese, F.; Lubitz, W. Biological Water Oxidation. *Acc. Chem. Res.* **2013**, *46*, 1588−1596.

(5) Park, S.; Shao, Y.; Liu, J.; Wang, Y. Oxygen electrocatalysts for water electrolyzers and reversible fuel cells: status and perspective. *Energy Environ. Sci.* **2012**, *5*, 9331−9344.

(6) Coggins, M. K.; Sun, X.; Kwak, Y.; Solomon, E. I.; Rybak-Akimova, E.; Kovacs, J. A. Characterization of Metastable Intermediates Formed in the Reaction Between a Mn(II) Complex and Dioxygen, Including a Crystallographic Structure of a Binuclear Mn(III)-Peroxo Species. *J. Am. Chem. Soc.* **2013**, *135*, 5631−5640.

(7) Geiger, R. A.; Wijeratne, G.; Day, V. W.; Jackson, T. A. Steric and Electronic Influences on the Structures of Peroxomanganese(III) Complexes Supported by Tetradentate Ligands. *Eur. J. Inorg. Chem.* **2012**, *10*, 1598−1608.

(8) Chattopadhyay, S.; Geiger, R. A.; Yin, G.; Busch, D. H.; Jackson, T. A. Oxo- and Hydroxomanganese(IV) Adducts: A Comparative Spectroscopic and Computational Study. *Inorg. Chem.* **2010**, *49*, 7530−7535.

(9) Geiger, R. A.; Leto, D. F.; Chattopadhyay, S.; Dorlet, P.; Anxolabéhère-Mallart, E.; Jackson, T. A. Geometric and Electronic Structures of Peroxomanganese(III) Complexes Supported by Pentadentate Amino-Pyridine and -Imidazole Ligands. *Inorg. Chem.* **2011**, *50*, 10190−10203.

(10) Shook, R. L.; Gunderson, W. A.; Greaves, J.; Ziller, J. W.; Hendrich, M. P.; Borovik, A. S. A Monomeric MnIII-Peroxo Complex Derived Directly from Dioxygen. *J. Am. Chem. Soc.* **2008**, *130*, 8888−8889.

(11) Rees, J. A.; Martin-Diaconescu, V.; Kovacs, J. A.; DeBeer, S. X-ray Absorption and Emission Study of Dioxygen Activation by a Small-Molecule Manganese Complex. *Inorg. Chem.* **2015**, *54*, 6410−6422.

(12) Bossek, U.; Weyhermuller, T.; Wieghardt, K.; Nuber, B.; Weiss, J. [L2Mn2(mu-O)2(mu-02)](ClO4): The First Binuclear (muPeroxo) dimanganese(IV) Complex (L= 1,4,7-Trimethyl- 1,4,7triazacyclononane). A Model for the S4 - So Transformation in the Oxygen Evolving Complex in Photosynthesis. *J. Am. Chem. Soc.* **1990**, *112*, 6387−6388.

(13) Lee, J. Y.; Karlin, K. D. Elaboration of copper-oxygen mediated C-H activation chemistry in consideration of future fuel and feedstock generation. *Curr. Opin. Chem. Biol.* **2015**, *25*, 184−193.

DOI: 10.1021/jacs.9b04729
J. Am. Chem. Soc. 2019, 141, 15046−15057

(14) Lewis, E. A.; Tolman, W. B. Reactivity of dioxygen-copper systems. *Chem. Rev.* **2004**, *104*, 1047−1076.
(15) Tinberg, C. E.; Lippard, S. J. Dioxygen Activation in Soluble Methane Monooxygenase. *Acc. Chem. Res.* **2011**, *44*, 280−288.
(16) Solomon, E. I.; Wong, S. D.; Liu, L. V.; Decker, A.; Chow, M. S. Peroxo and oxo intermediates in mononuclear non-heme iron enzymes and related active sites. *Curr. Opin. Chem. Biol.* **2009**, *13*, 99−113.
(17) Green, M. T. C-H bond activation in heme proteins: the role of thiolate ligation in cytochrome P450. *Curr. Opin. Chem. Biol.* **2009**, *13*, 84−88.
(18) Costas, M.; Mehn, M. P.; Jensen, M. P.; Que, L. J. Dioxygen Activation at Mononuclear Nonheme Iron Active Sites: Enzymes, Models, and Intermediates. *Chem. Rev.* **2004**, *104*, 939−986.
(19) Solomon, E. I.; Heppner, D. E.; Johnston, E. M.; Ginsbach, J. W.; Cirera, J.; Qayyum, M.; Kieber-Emmons, M. T.; Kjaergaard, C. H.; Hadt, R. G.; Tian, L. Copper Active Sites in Biology. *Chem. Rev.* **2014**, *114*, 3659−3853.
(20) Renger, G. Light induced oxidative water splitting in photosynthesis: Energetics, kinetics and mechanism. *J. Photochem. Photobiol., B* **2011**, *104*, 35−43.
(21) Retegan, M.; Krewald, V.; Mamedov, F.; Neese, F.; Lubitz, W.; Cox, N.; Pantazis, D. A. A five-coordinate Mn(IV) intermediate in biological water oxidation: spectroscopic signature and a pivot mechanism for water binding. *Chem. Sci.* **2016**, *7*, 72−84.
(22) Cox, N.; Retegan, M.; Neese, F.; Pantazis, D. A.; Boussac, A.; Lubitz, W. Electronic structure of the oxygen evolving complex in photosystem II prior to O-O bond formation. *Science* **2014**, *345*, 804−808.
(23) Brudvig, G. W. Water oxidation chemistry of photosystem II. *Philos. Trans. R. Soc., B* **2008**, *363*, 1211−1219.
(24) Dismukes, G. C.; Brimblecombe, R.; Felton, G. A. N.; Pryadun, R. S.; Sheats, J. E.; Spiccia, L.; Swiegers, G. F. Development of Bioinspired Mn4O4-Cubane Water Oxidation Catalysts: Lessons from Photosynthesis. *Acc. Chem. Res.* **2009**, *42*, 1935−1943.
(25) Betley, T. A.; Wu, Q.; Van Voorhis, T.; Nocera, D. G. Electronic Design Criteria for O-O Bond Formation via Metal-Oxo Complexes. *Inorg. Chem.* **2008**, *47*, 1849−1861.
(26) Armstrong, F. A. Why did Nature Choose manganese to make oxygen? *Philos. Trans. R. Soc., B* **2008**, *363*, 1263−1270.
(27) Shearer, J.; Scarrow, R. C.; Kovacs, J. A. Synthetic models for the cysteinate-ligated Non-Heme Iron Enzyme Superoxide Reductase: Observation and Structural characterization by XAS of an FeIII-OOH Intermediate. *J. Am. Chem. Soc.* **2002**, *124*, 11709−11717.
(28) Kitagawa, T.; Dey, A.; Lugo-Mas, P.; Benedict, J.; Kaminsky, W.; Solomon, E.; Kovacs, J. A. A Functional Model for the Metalloenzyme Superoxide Reductase. *J. Am. Chem. Soc.* **2006**, *128*, 14448−14449.
(29) Nam, E.; Alokolaro, P. E.; Swartz, R. D.; Gleaves, M. C.; Pikul, J.; Kovacs, J. A. An Investigation of the Mechanism of Formation of a Thiolate-Ligated Fe(III)-OOH. *Inorg. Chem.* **2011**, *50*, 1592−1602.
(30) Kovacs, J. A.; Brines, L. M. Understanding How the Thiolate Sulfur Contributes to the Function of the Non-Heme Iron Enzyme Superoxide Reductase. *Acc. Chem. Res.* **2007**, *40* (7), 501−9.
(31) Villar-Acevedo, G.; Nam, E.; Fitch, S.; Benedict, J.; Freudenthal, J.; Kaminsky, W.; Kovacs, J. A. Influence of Thiolate Ligands on Reductive N-O Bond Activation. Oxidative Addition of NO to a Biomimetic SOR Analogue, and its Proton-Dependent Reduction of Nitrite. *J. Am. Chem. Soc.* **2011**, *133*, 1419−1427.
(32) Brown, C. D.; Neidig, M. L.; Neibergall, M. B.; Lipscomb, J. D.; Solomon, E. I. VTVH-MCD and DFT Studies of Thiolate Bonding to {FeNO}7/{FeO2}8 Complexes of Isopenicillin N Synthase: Substrate Determination of Oxidase versus Oxygenase Activity in Nonheme Fe Enzymes. *J. Am. Chem. Soc.* **2007**, *129* (23), 7427−7438.
(33) Blakely, M. N.; Dedushko, M. A.; Yan Poon, P. C.; Villar-Acevedo, G.; Kovacs, J. A. Formation of a Reactive, Alkyl Thiolate-Ligated FeIII-Superoxo Intermediate Derived from Dioxygen. *J. Am. Chem. Soc.* **2019**, *141*, 1867−1870.
(34) Kovacs, J. A. How Iron Activates O2. *Science* **2003**, *299*, 1024−1025.
(35) Pecoraro, V. L.; Baldwin, M. J.; Gelasco, A. Interaction of Manganese with Dioxygen and Its Reduced Derivatives. *Chem. Rev.* **1994**, *94*, 807−826.
(36) Guo, M.; Lee, Y.-M.; Gupta, R.; Seo, M. S.; Ohta, T.; Wang, H.-H.; Liu, H.-Y.; Dhuri, S. N.; Sarangi, R.; Fukuzumi, S.; Nam, W. Dioxygen Activation and O−O Bond Formation Reactions by Manganese Corroles. *J. Am. Chem. Soc.* **2017**, *139*, 15858−15867.
(37) Crandell, D. W.; Xu, S.; Smith, J. M.; Baik, M.-H. Intramolecular Oxyl Radical Coupling Promotes O−O Bond Formation in a Homogeneous Mononuclear Mn-based Water Oxidation Catalyst: A Computational Mechanistic Investigation. *Inorg. Chem.* **2017**, *56*, 4435−4445.
(38) Liao, R.-Z.; Siegbahn, P. E. M. Quantum Chemical Modeling of Homogeneous Water Oxidation Catalysis. *ChemSusChem* **2017**, *10*, 4236−4263.
(39) Kim, S. H.; Park, H.; Seo, M. S.; Kamachi, T.; Kubo, M.; Ogura, T.; Klajn, J.; Gryko, D. T.; Valentine, J. S.; Nam, W. Reversible O-O Bond Cleavage and Formation between Mn(IV)-Peroxo and Mn(V)-Oxo Corroles. *J. Am. Chem. Soc.* **2010**, *132*, 14030−14032.
(40) Ray, K.; Pfaff, F. F.; Wang, B.; Nam, W. Status of Reactive Non-Heme Metal-Oxygen Intermediates in Chemical and Enzymatic Reactions. *J. Am. Chem. Soc.* **2014**, *136*, 13942−13958.
(41) Jones, R. D.; Summerville, D. A.; Basolo, F. Manganese(II) Porphyrin Oxygen Carriers. Equilibrium Constants for the Reaction of Dioxygen with Para-Substituted meso-Tetraphenylporphinatomanganese(II) Complexes. *J. Am. Chem. Soc.* **1978**, *100*, 4416−4424.
(42) Seo, M. S.; Kim, J. Y.; Annaraj, J.; Kim, Y.; Lee, Y.-M.; Kim, S.-J.; Kim, J.; Nam, W. [Mn(tmc)(O2)]+: A Side-On Peroxido Manganese(III) Complex Bearing a Non-Heme Ligand. *Angew. Chem., Int. Ed.* **2007**, *46*, 377−380.
(43) VanAtta, R. B.; Strouse, C. E.; Hanson, L. K.; Valentine, J. S. [Peroxotetraphenylporphinato]manganese(III) and [Chlorotetraphenylporphinato]manganese(II) Anions. Syntheses, Crystal Structures, and Electronic Structures. *J. Am. Chem. Soc.* **1987**, *109*, 1425−1434.
(44) Kitajima, N.; Komatsuzaki, H.; Hikichi, S.; Osawa, M.; Moro-Oka, Y. A Monomeric Side-On Peroxo Manganese(III) Complex: Mn(o2)(3,5-iPr2pzH)(HB(3,5-iPrzpz)3). *J. Am. Chem. Soc.* **1994**, *116*, 11596−11597.
(45) Singh, U. P.; Sharma, A. K.; Hikichi, S.; Komatsuzaki, H.; Moro-Oka, Y.; Akita, M. Hydrogen bonding interaction between imidazolyl N-H group and peroxide: Stabilization of Mn(III)-peroxo complexTpiPr2Mn(g2-O2)(imMeH) (imMeH = 2-methylimidazole). *Inorg. Chim. Acta* **2006**, *359*, 4407−4411.
(46) So, H.; Park, Y. J.; Cho, K.-B.; Lee, Y.-M.; Seo, M. S.; Cho, J.; Sarangi, R.; Nam, W. Spectroscopic Characterization and Reactivity Studies of a Mononuclear Nonheme Mn(III)−Hydroperoxo Complex. *J. Am. Chem. Soc.* **2014**, *136*, 12229−12232.
(47) Kovacs, J. A. Tuning the Relative Stability and Reactivity of Manganese Dioxygen and Peroxo Intermediates via Systematic Ligand Modification. *Acc. Chem. Res.* **2015**, *48*, 2744−2753.
(48) Coggins, M. K.; Toledo, S.; Shaffer, E.; Kaminsky, W.; Shearer, J.; Kovacs, J. A. Characterization and dioxygen reactivity of a new series of coordinatively unsaturated thiolate-ligated manganese(II) complexes. *Inorg. Chem.* **2012**, *51* (12), 6633−44.
(49) Coggins, M. K.; Martin-Diaconescu, V.; De Beer, S.; Kovacs, J. A. Correlation Between Structural, Spectroscopic, and Reactivity Properties Within a Series of Structurally Analogous Metastable Manganese(III)-Alkylperoxo Complexes. *J. Am. Chem. Soc.* **2013**, *135*, 4260−4272.
(50) Rybak-Akimova, E. V.; Otto, W.; Deardorf, P.; Roesner, R.; Busch, D. H. Kinetics and Equilibrium of Dioxygen Binding to a Vacant Site in Cobalt(II) Complexes with Pentadentate Ligands. *Inorg. Chem.* **1997**, *36*, 2746−2753.
(51) Antonini, E.; Brunori, M. *Hemoglobin and Myoglobin in Their Reactions with Ligands*; North-Holland: Amsterdam, 1971.
(52) Liu, L. V.; Hong, S.; Cho, J.; Nam, W.; Solomon, E. I. Comparison of High-Spin and Low-Spin Nonheme FeIII−OOH

DOI: 10.1021/jacs.9b04729
J. Am. Chem. Soc. 2019, 141, 15046−15057

Complexes in O−O Bond Homolysis and H Atom Abstraction Reactivities. *J. Am. Chem. Soc.* **2013**, *135*, 3286−3299.
(53) Eliel, E. L.; Wilen, S. H.; Mander, L. N. *Stereochemistry of Organic Compounds*; Wiley: New York, 1994.
(54) Coggins, M. K.; Martin-Diaconescu, V.; DeBeer, S.; Kovacs, J. A. Correlation between structural, spectroscopic, and reactivity properties within a series of structurally analogous metastable manganese(III)-alkylperoxo complexes. *J. Am. Chem. Soc.* **2013**, *135* (11), 4260−72.
(55) Coggins, M. K.; Kovacs, J. A. Structural and Spectroscopic Characterization of Metastable Thiolate-Ligated Manganese(III)-Alkylperoxo Species. *J. Am. Chem. Soc.* **2011**, *133*, 12470−12473.
(56) Krewald, V.; Lassalle-Kaiser, B.; Boron, T. T., III; Pollock, C. J.; Kern, J.; Beckwith, M. A.; Yachandra, V. K.; Pecoraro, V. L.; Yano, J.; Neese, F.; DeBeer, S. The Protonation States of Oxo-Bridged MnIV Dimers Resolved by Experimental and Computational Mn K Pre-Edge X ray Absorption Spectroscopy. *Inorg. Chem.* **2013**, *52*, 12904−12914.
(57) Larson, E. J.; Pecoraro, V. L. The Peroxide-Dependent μ2−0 Bond Formation of [MnIVSALPN(0)]2. *J. Am. Chem. Soc.* **1991**, *113*, 3810−3818.
(58) Caudle, M. T.; Kampf, J. W.; Kirk, M. L.; Rasmussen, P. G.; Pecoraro, V. L. The First Binuclear Mn(IV) Complex Containing a Bridging Imidazolate Ligand Exhibits Unique EPR Spectral Features. *J. Am. Chem. Soc.* **1997**, *119*, 9297−9298.
(59) Stoll, S.; Schweiger, A. EasySpin, a Comprehensive Software Package for Spectral Simulation and Analysis in EPR. *J. Magn. Reson.* **2006**, *178*, 42−55.
(60) Cotruvo, J. A., Jr.; Stich, T. A.; Britt, R. S.; Stubbe, J. Mechanism of Assembly of the Dimanganese-Tyrosyl Radical Cofactor of Class Ib Ribonucleotide Reductase: Enzymatic Generation of Superoxide Is Required for Tyrosine Oxidation via a Mn(III)Mn(IV) Intermediate. *J. Am. Chem. Soc.* **2013**, *135*, 4027−4039.
(61) Triller, M. U.; Hsieh, W. Y.; Pecoraro, V. L.; Rompel, A.; Krebs, B. Preparation of highly efficient manganese catalase mimics. *Inorg. Chem.* **2002**, *41* (21), 5544−5554.
(62) Glerup, J.; Goodson, P. A.; Hazell, A.; Hazell, R.; Hodgson, D. J.; Mckenzie, C. J.; Michelsen, K.; Rychlewska, U.; Toftlund, H. Synthesis and Characterization of Bis(Mu-Oxo)Dimanganese(Iii,Iii), Bis(Mu-Oxo)Dimanganese(Iii,Iv), and Bis(Mu-Oxo)Dimanganese(Iv,Iv) Complexes with Ligands Related to N,N'-Bis(2-Pyridylmethyl)-1,2-Ethanediamine (Bispicen). *Inorg. Chem.* **1994**, *33* (18), 4105−4111.
(63) Gupta, R.; Taguchi, T.; Lassalle-Kaiser, B.; Bominaar, E. L.; Yano, J.; Hendrich, M. P.; Borovik, A. S. High-spin Mn-oxo complexes and their relevance to the oxygen-evolving complex within photosystem II. *Proc. Natl. Acad. Sci. U. S. A.* **2015**, *112*, 5319−5324.
(64) Parsell, T. H.; Behan, R. K.; Green, M. T.; Hendrich, M. P.; Borovik, A. S. Preparation and Properties of a Monomeric Mn(IV)-Oxo Complex. *J. Am. Chem. Soc.* **2006**, *128*, 8728−8729.
(65) Ivancich, A.; Barynin, V. V.; Zimmermann, J.-L. Pulsed EPR Studies of the Binuclear Mn(III)Mn(IV) Center in Catalase from Thermus themophilus. *Biochemistry* **1995**, *34*, 6628−6639.
(66) Randall, D. W.; Gelasco, A.; Caudle, M. T.; Pecoraro, V. L.; Britt, R. D. ESE-ENDOR and ESEEM Characterization of Water and Methanol Ligation to a Dinuclear Mn(III)Mn(IV) Complex. *J. Am. Chem. Soc.* **1997**, *119*, 4481−4491.

DOI: 10.1021/jacs.9b04729
J. Am. Chem. Soc. 2019, 141, 15046−15057